

NAVAL POSTGRADUATE SCHOOL

Monterey, California



THESIS

**PARABOLIC EQUATION MODELING OF BOTTOM
INTERFACE AND VOLUME REVERBERATION IN
SHALLOW WATER**

by

Li, Lit Siew

September 2000

Thesis Advisor:
Second Reader:

Kevin B. Smith
James V. Sanders

Approved for public release; distribution is unlimited.

DTIC QUALITY INSPECTED 4

20001222 098

REPORT DOCUMENTATION PAGE			Form Approved OMB No. 0704-0188	
Public reporting burden for this collection of information is estimated to average 1 hour per response, including the time for reviewing instruction, searching existing data sources, gathering and maintaining the data needed, and completing and reviewing the collection of information. Send comments regarding this burden estimate or any other aspect of this collection of information, including suggestions for reducing this burden, to Washington Headquarters Services, Directorate for Information Operations and Reports, 1215 Jefferson Davis Highway, Suite 1204, Arlington, VA 22202-4302, and to the Office of Management and Budget, Paperwork Reduction Project (0704-0188) Washington DC 20503.				
1. AGENCY USE ONLY (Leave blank)		2. REPORT DATE September 2000		3. REPORT TYPE AND DATES COVERED Master's Thesis
4. TITLE AND SUBTITLE Parabolic Equation Modeling of Bottom Interface and Volume Reverberation in Shallow Water			5. FUNDING NUMBERS	
6. AUTHOR(S) LI, LIT SIEW				
7. PERFORMING ORGANIZATION NAME(S) AND ADDRESS(ES) Naval Postgraduate School Monterey CA 93943-5000			8. PERFORMING ORGANIZATION REPORT NUMBER	
9. SPONSORING/MONITORING AGENCY NAME(S) AND ADDRESS(ES)			10. SPONSORING/MONITORING AGENCY REPORT NUMBER	
11. SUPPLEMENTARY NOTES The views expressed in this thesis are those of the author and do not reflect the official policy or position of the Department of Defense or the U.S. Government.				
12a. DISTRIBUTION/AVAILABILITY STATEMENT Approved for public release; distribution is unlimited.			12b. DISTRIBUTION CODE	
13. ABSTRACT (maximum 200 words) A reverberation model based on the parabolic approximation is developed that includes sediment interface and volume perturbations. A multiple forward/single backscatter approximation is made, and the structure of the solution is found to depend on the two-way propagation with a scattering strength scaling dependent on the local properties of the perturbation. The model is implemented for continuous wave (CW) signals to predict mean reverberation pressure levels and for broadband pulse signals to generate complex reverberation structures in the time-domain. The spatial correlation and statistical properties of these predicted signals are then analyzed in an attempt to extract information on the underlying characteristics of the perturbation. Preliminary analysis suggests that reverberation due to the volume perturbations decorrelates more rapidly over depth than the reverberation due to interface fluctuations, although the differences appear small. Additionally, the statistical character of the reverberation structure due to the interface appears as a relatively flat spectrum, while the spectrum of the volume reverberation tends to appear colored. Attempts to correlate these characteristics with the structure of the perturbations is ongoing.				
14. SUBJECT TERMS: Shallow-water sound propagation, reverberation, bottom interface, bottom volume, spatial perturbations, sound speed perturbations, peak correlations, time/temporal series, range series, MMPE, MMPEREV			15. NUMBER OF PAGES 142	
			16. PRICE CODE	
17. SECURITY CLASSIFICATION OF REPORT Unclassified	18. SECURITY CLASSIFICATION OF THIS PAGE Unclassified	19. SECURITY CLASSIFICATION OF ABSTRACT Unclassified	20. LIMITATION OF ABSTRACT UL	

NSN 7540-01-280-5500

Standard Form 298 (Rev. 2-89)
Prescribed by ANSI Std. Z39-18 298-102

Approved for public release; distribution is unlimited.

**PARABOLIC EQUATION MODELING OF BOTTOM INTERFACE AND
VOLUME REVERBERATION IN SHALLOW WATER**

Li, Lit Siew

**Major, Republic of Singapore Navy
B. Eng(Elect)(Honours Second Class Upper Division)
Nanyang Technological University, Singapore, 1992**

**Submitted in partial fulfilment
of the requirements for the degree of**

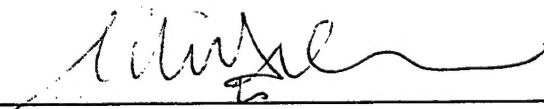
MASTER OF SCIENCE IN ENGINEERING ACOUSTICS

from the

NAVAL POSTGRADUATE SCHOOL

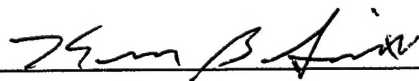
September 2000

Author:

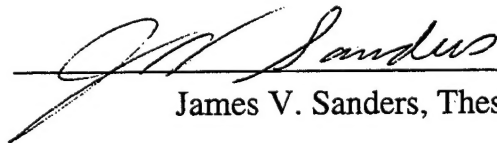


Li, Lit Siew

Approved by:



Kevin B. Smith, Thesis Advisor



James V. Sanders, Thesis Second Reader



**Kevin B. Smith, Chairman
Engineering Acoustics Academic Group**

ABSTRACT

A reverberation model based on the parabolic approximation is developed that includes sediment interface and volume perturbations. A multiple forward/single backscatter approximation is made, and the structure of the solution is found to depend on the two-way propagation with a scattering strength scaling dependent on the local properties of the perturbation. The model is implemented for continuous wave (CW) signals to predict mean reverberation pressure levels and for broadband pulse signals to generate complex reverberation structures in the time-domain. The spatial correlation and statistical properties of these predicted signals are then analyzed in an attempt to extract information on the underlying characteristics of the perturbation. Preliminary analysis suggests that reverberation due to the volume perturbations decorrelates more rapidly over depth than the reverberation due to interface fluctuations, although the differences appear small. Additionally, the statistical character of the reverberation structure due to the interface appears as a relatively flat spectrum, while the spectrum of the volume reverberation tends to appear colored. Attempts to correlate these characteristics with the structure of the perturbations is ongoing.

TABLE OF CONTENTS

I. INTRODUCTION	1
II. THE REVERBERATION PROBLEM – SHALLOW WATER REVERBERATION AND SCATTERING THEORY.....	5
A. BOTTOM INTERFACE SCATTERING	5
1. Forward Propagation	10
2. Backward Propagation	10
3. Forcing Function	11
4. Statistical Treatment of the Scattered Field	14
5. Mean Squared Reverberation Pressure Level, RPL	19
B. VOLUME SCATTERING	21
C. TIME-DOMAIN ANALYSIS.....	26
1. Time-Domain Analysis of the Interface.....	26
2. Time-Domain Analysis of the Volume	30
III. GENERATING REALIZATIONS – IMPLEMENTATION OF THE REVERBERATION PROBLEM IN MMPE	33
A. SPECTRAL DESCRIPTIONS OF BOTTOM VARIABILITY	33
1. Interface Roughness (Spatial Perturbation).....	33
2. Volume Sound Speed Fluctuations	36
3. Spectral Filter	39
B. IMPLEMENTATION OF THE INTERFACE AND VOLUME SPECTRAL DESCRIPTIONS IN MMPE.....	40
1. Description of MMPE	40
2. FORTRAN & MATLAB Implementation of Perturbation Models....	41
3. Results of Varying RMS Values to Perturbations.....	41
IV. POST-PROCESSING IMPLEMENTATIONS IN MATLAB AND SIMULATION RESULTS	47
A. MODELING ENVIRONMENT AND GEOMETRY	48
1. Multi-static Reverberation Geometry.....	48
2. The Environment.....	49
3. MMPE and MMPEREV Runs	53
B. POST-PROCESSING 1 – REVERBERATION (MATLAB IMPLEMENTATION).....	55
1. Two-way Mono/Bistatic CW Reverberation Analysis.....	55
2. CW Analysis Results.....	57
3. Two-way Mono/Bistatic Time-Domain Reverberation Analysis	62
4. Time-Domain Analysis Results	63
5. MATLAB Data Analysis.....	68

C. POST-PROCESSING 2 – VERTICAL CORRELATION & PEAK CORRELATION IN CW AND TIME-DOMAIN	68
1. Vertical Correlation in Range & Peak Vertical Correlation.....	69
2. Vertical Temporal Correlation & Peak Vertical Temporal Correlation.....	72
D. POST-PROCESSING 3 – SPECTRAL ANALYSES	76
1. Signal Analysis 1 – Power Spectral Density	80
2. Signal Analysis 2 – Power Ratio Spectral Density	83
V. CONCLUSIONS & RECOMMENDATIONS	87
LIST OF REFERENCES	89
INITIAL DISTRIBUTION LIST	91

ACKNOWLEDGEMENTS

I see the completion of this thesis as the culmination of the eighteen months I have spent at the Naval Postgraduate School. Everything from the school's aura to the familiarity of the Advanced Acoustic Research Laboratory are all part of the successful completion my endeavour for a M.Sc. in Engineering Acoustics at NPS. This thesis in particular caps the conclusion with a special sense of satisfaction.

I wish therefore to thank firstly, my God, for His grace and mercy. My wife, Sandra and the boys, Daniel and Justin, for without them my studies in the Naval Postgraduate School would not have been possible. I have continually drawn strength from them who have been the constant in my life. I cannot also imagine how it would be like without them all by my side during this significant period of my life. Kudos to Sandra especially for her fortitude, patience and 'saneness' in all the madness I have put her and the boys through!

Professor Kevin B. Smith, who introduced and taught me much about sound propagation and the 'do's and don'ts' of the MMPE model, which I still do not fully understand – my heartfelt thanks. He also spent hours debugging errant MATLAB codes testifying to his hands-on approach to advising his students. His practical and cool demeanour has given me freedom yet close guidance.

Thanks go also to Professor James V. Sanders, Academic Associate and Second Reader who with patience has given constant assurance of my pursuit. To Commander James R. Hill my Curricula Officer and Professor James N. Eagle, Undersea Warfare Academic Group Chairman, who together with Prof. Sanders have given me tremendous latitude and freedom throughout my endeavour.

Monterey will always remain a part of us.

I. INTRODUCTION

In 1993, the Office of Naval Research (ONR) sponsored a reverberation program, the Acoustic Reverberation Special Research Program (ARSRP), to study the primary causes and nature of acoustic reverberation in the deep ocean. The region studied was near the Mid-Atlantic Ridge, an area where bottom characteristics are dominated by highly variable topography and hard, basaltic rock structures (Tucholke, et al, 1993a and 1993b). The dominant feature contributing to long-range reverberation was then the water/bottom interface. Furthermore, the general structure of the reverberation signal was found to correlate quite well with the forward propagation (Smith, et al., 1996, and Makris, et al., 1994), i.e. high reverberation returns were found to occur where energy interacted strongly with the bottom.

Previous analysis with a broadband parabolic equation (PE) model has shown good agreement with predicted arrival time structures due to deep-ocean bottom interface reverberation (Smith and Cushman, 1997). Application of this approach for both single frequency (CW) and broadband pulse propagation calculations showed good agreement with measured data. In addition, the broadband reverberation predictions indicated that some features of the reverberation signal required the discrimination of multipath propagation in order to fully resolve the structure, particularly in CW shadow zones.

A reverberation experiment is now being organized by ONR in the littoral regions of the East and South China Seas called ASIAEX. In contrast to the previous deep ocean regions studied, this area has a much smoother and softer water/bottom interface. It is unclear at this point whether the dominant mechanism for bottom reverberation will be interface roughness or volume inhomogeneities in the sediment. One may expect that the measured reverberation will contain statistical information related to the character of the scattering mechanism. However, the reverberation signal from the sediment volume may

be affected by forward scatter from the interface and vice-versa, thereby complicating the distinction of the dominant mechanism.

The purpose of the present work is to establish a model for predicting the influence of propagation on both interface and volume reverberation in a shallow water environment. This model is similar to the previous PEREV model (Tappert and Ryan, 1989), although it formally treats the scattering influence in the context of the PE approximation. It is further expanded to treat volume scattering.

Starting with based on the Monterey-Miami Parabolic Equation (MMPE) propagation model developed by Smith and Tappert (1994) and Smith (2000), bottom interface and sediment sound speed perturbations were incorporated and broadband and CW analysis conducted. The theoretical basis of reverberation due to the bottom interface and bottom volume is developed in Chapter II. Specifically, we were able to use a CW one-way propagation model to show that the reverberant field is the coupling of two, one-way propagations. The theoretical basis for reverberation was expanded to time-domain analysis for both the interface and volume in order to provide simulation for pulsed propagation. In this method, it was shown that the two, one-way propagations from the source to the scattering patch and from the receiver to the scattering patch would give the reverberation field by convolution of both fields in time. Chapter II also details the models used for generating realizations based on statistically controlled random fluctuations for the interface and volume, and offer a practical implementation that was incorporated into the MMPE model. This new model is known as MMPEREV (see Chapter III).

Secondly, after incorporating random fluctuations of pertinent parameters into the MMPE model, post-processing analysis of these results in MATLAB was performed. Chapter IV describes the post-processing and signal processing implemented in MATLAB and provides a visual presentation of the effects of reverberation. A single set of environmental parameters was used in all the simulations to afford a controlled computation of the effects of reverberation, providing a qualitative description of the

analysis. Comparisons between perturbed and unperturbed data were conducted and detailed in Chapter IV. Post-processing and signal analysis included:

- time-domain analysis and comparison with unperturbed results;
- CW analysis and comparison with unperturbed results;
- temporal and range peak auto- and cross-correlations in depth;
- spectral analyses of the reverberation and reverberation loss.

This model will serve as a tool for understanding propagation influences in future reverberation experiments.

THIS PAGE IS INTENTIONALLY LEFT BLANK

II. THE REVERBERATION PROBLEM – SHALLOW WATER REVERBERATION AND SCATTERING THEORY

In this chapter, we present a theoretical treatment of the effects of bottom reverberation and scattering. We acknowledge that in shallow water, the effects of reverberation are more involved due to the thin layer of water and the somewhat invariant sound speed profile in the water column. However, perturbations to the interface and sediment volume (hereafter known as just the ‘volume’) exist and may be modeled statistically. These will be treated in detail. One element lacking at this point is the study into density variabilities in the volume. Implementation for density variability will form part of the scope of follow-on work, which is discussed in Chapter V.

The interface and volume perturbations may be treated separately because of the nature of their perturbations – the interface primarily being perturbed spatially while the volume variabilities involve both the sound speed and density. In order to effectively model their total effects, all interface and volume perturbations must be jointly incorporated into the model at the same time. This has been integrated into the MMPE Model developed by Smith, 2000 (originally known as the UMPE Model developed by Smith and Tappert, 1994).

A. BOTTOM INTERFACE SCATTERING

We begin with the standard wave equation, also known as the Helmholtz wave equation. It is written for acoustic pressure, p , as

$$\nabla^2 p + k_0^2 n^2 p = 0 \quad (2.1)$$

with the following definitions for wavenumber and index of refraction, including the reference sound speed,

$$k_0 = \omega / c_0 \text{ and } n(\vec{x}) = c_0 / c(\vec{x}). \quad (2.2)$$

Now, consider a rough bottom where the spatial fluctuations may be defined statistically. The boundary between the water column and the bottom is then defined by,

$$n^2 = n_w^2(1 - H(z - z_b)) + n_b^2 H(z - z_b), \quad (2.3)$$

where n_w and n_b represent the spatially varying indices of refraction in the water column and bottom (volume), respectively, and z_b is the bathymetric depth at the interface. The definition of the Heaviside step function used at the water/bottom interface is given by

$$H(z) = \begin{cases} 1, & z > 0 \\ 1/2, & z = 0 \\ 0, & z < 0 \end{cases}, \text{ and } \frac{\partial}{\partial z} H(z) = \delta(z). \quad (2.4)$$

We treat the influence of the roughness of the bottom interface by introducing perturbations to the bottom depth of varying length scales. This is akin to the method of small perturbations (MSP) found in Brekhovskikh and Lysanov (1990). More specifically, we define

$$z_b(\vec{r}) = \bar{z}_b(\vec{r}) + \eta_l(\vec{r}) + \eta_s(\vec{r}), \quad (2.5)$$

where $\bar{z}_b(\vec{r})$ is the deterministic portion of the bathymetry as a function of horizontal range, \vec{r} . The deterministic part of the bathymetry may also be seen as the mean depth on a relatively flat portion of the seabed. Correspondingly, $\eta_l(\vec{r})$ is the long-wavelength portion of the randomly generated roughness comprising a spectrum of roughness, while $\eta_s(\vec{r})$ is the short-wavelength component, also generated randomly. The short-wavelength components are assumed to be the components generating scatter, thereby responsible for reverberation, predominantly at the Bragg wavenumber. The short wavelength components may be thought of as the easily observable variability of the seafloor, i.e. loose impediments and small mounts. The longer wavelengths are then the larger undulations. Hence, it is reasonable to think of a 'critical' or 'limiting' wavenumber separating these two components. This critical or limiting wavenumber is assumed to be approximately, $k_{\text{lim}} \approx \frac{1}{2} k_0 \theta_c^2$, where θ_c is the critical angle of

propagation, and smaller roughness wavenumbers (i.e. longer wavelengths) are assumed to dominate the forward scatter properties of the acoustic field.

Performing a Taylor series expansion of the Heaviside step function we have defined in Eq. (2.4), we can then re-write the original Helmholtz equation, Eq. (2.1), as

$$\nabla^2 p + k_0^2(\hat{n}^2 + \mu)p = 0 \quad (2.6a)$$

where

$$\hat{n}^2 = n_w^2(1 - H(z - \bar{z}_b - \eta_l)) + n_b^2 H(z - \bar{z}_b - \eta_l) \quad (2.6b)$$

and

$$\mu(\bar{r}, z) = (n_w^2 - n_b^2)\eta_s \delta(z - \bar{z}_b - \eta_l). \quad (2.6c)$$

This shows that the primary part of the propagation is due to the long-wavelength components and the perturbation is due to the small wavelength components. The small-scale features previously expressed as $\eta_s(\bar{r})$ are considered to introduce secondary cross-terms whose contribution will be small and may thus be ignored. From hereon, ignoring the short-wavelength components will introduce an approximation to the theoretical development and variables will then be "hatted" to denote the use of only long-wavelength perturbations, e.g., the approximate refractive index, \hat{n} .

We now express the wave equation in cylindrical coordinates as

$$\left[\frac{1}{r} \frac{\partial}{\partial r} \left(r \frac{\partial}{\partial r} \right) + \frac{1}{r^2} \frac{\partial^2}{\partial \phi^2} + \frac{\partial^2}{\partial z^2} \right] p + k_0^2(\hat{n}^2 + \mu)p = 0. \quad (2.7)$$

Now let $p = \frac{1}{\sqrt{r}}u$, then

$$\frac{\partial^2 u}{\partial r^2} + \frac{1}{r^2} \frac{\partial^2 u}{\partial \phi^2} + \frac{\partial^2 u}{\partial z^2} + k_0^2(\hat{n}^2 + \mu)u = 0. \quad (2.8)$$

Next, we define the Q operator as

$$Q = \sqrt{\hat{n}^2 + \mu + \frac{1}{k_0^2} \left(\frac{1}{r^2} \frac{\partial^2}{\partial \phi^2} + \frac{\partial^2}{\partial z^2} \right)}. \quad (2.9)$$

In general, the azimuthal coupling is ignored in a $N \times 2D$ model by neglecting the $\frac{\partial^2}{\partial \phi^2}$ term. The influence of azimuthal coupling may be expected to be of second order, so the neglect of such influences here is consistent with the treatment of small perturbations.

The wave equation now becomes

$$\frac{\partial^2 u}{\partial r^2} + k_0^2 Q^2 u = 0. \quad (2.10)$$

Defining u in terms of its incoming and outgoing components, Tappert (1977) showed that we may write it in the form

$$u = \frac{1}{\sqrt{Q}}(u_+ + u_-), \quad \text{and} \quad \frac{\partial u}{\partial r} = ik_0 \sqrt{Q}(u_+ - u_-). \quad (2.11)$$

The wave equations defining the evolutions of the outgoing and incoming fields can then be shown to satisfy

$$\frac{\partial u_+}{\partial r} \approx ik_0 Q u_+ + \frac{1}{2} \frac{\partial Q}{\partial r} u_+, \quad \text{and} \quad \frac{\partial u_-}{\partial r} \approx -ik_0 Q u_- + \frac{1}{2} \frac{\partial Q}{\partial r} u_-. \quad (2.12)$$

This shows how the fields form a set of coupled, one-way parabolic wave equations.

Since the employment of an operator, Q , is not algebraic and therefore inconvenient, we invoke the wide-angle parabolic approximation (Thomson and Chapman, 1983) and define Q_{WAPE} ,

$$Q \approx Q_{WAPE} = \sqrt{1 + \frac{1}{k_0^2} \frac{\partial^2}{\partial z^2}} + \left[(n^2 + \mu)^{1/2} - 1 \right], \quad (2.13)$$

We can re-write it in terms of a Hamiltonian differential operator, H_{WAPE} ,

$$Q_{WAPE} = 1 - (T + U) = 1 - H_{WAPE}(r, z, \frac{\partial^2}{\partial z^2}), \quad (2.14a)$$

where,

$$H_{WAVE}\left(r, z, \frac{\partial^2}{\partial z^2}\right) = T + U \quad (2.14b)$$

is written in terms of kinetic and potential operators,

$$T = 1 - \sqrt{1 + \frac{1}{k_0^2} \frac{\partial^2}{\partial z^2}} \quad (2.14c)$$

and

$$U = -\left[(\hat{n}^2 + \mu)^{1/2} - 1\right]. \quad (2.14d)$$

Since we expect μ to be small,

$$U \approx -(\hat{n} + \frac{1}{2} \frac{\mu}{\hat{n}} - 1) = \hat{U}(r, z) - \frac{1}{2} \frac{\mu}{\hat{n}}, \quad (2.15)$$

where we have also defined

$$\hat{U}(r, z) = -(\hat{n}(r, z) - 1) \quad (2.16)$$

as the unperturbed potential function. Equation (2.14a) then becomes

$$Q_{WAVE} = 1 - \hat{H}_{WAVE}\left(r, z, \frac{\partial^2}{\partial z^2}\right) + \frac{1}{2} \frac{\mu(r, z)}{\hat{n}(r, z)} \quad (2.17)$$

since $\hat{H}_{WAVE}\left(r, z, \frac{\partial^2}{\partial z^2}\right) = (T + \hat{U})$.

Now, $\frac{\partial Q}{\partial r} \approx \frac{\partial Q_{WAVE}}{\partial r} \approx \frac{1}{2\hat{n}} \frac{\partial \mu}{\partial r}$ since the strongest range dependence is assumed in

μ . Then, the evolution of the outgoing and incoming fields from Eq. (2.12) becomes

$$\frac{\partial u_+}{\partial r} \approx ik_0 u_+ - ik_0 \hat{H}_{WAVE} u_+ + \frac{1}{4\hat{n}} \frac{\partial \mu}{\partial r} u_- , \quad \text{and} \quad (2.18a)$$

$$\frac{\partial u_-}{\partial r} \approx -ik_0 u_- + ik_0 \hat{H}_{WAVE} u_- + \frac{1}{4\hat{n}} \frac{\partial \mu}{\partial r} u_+ . \quad (2.18b)$$

From Eq. (2.18a) and (2.18b), the two fields are seen to couple through the third term on the right-hand-side of each equation. We now invoke the multiple-forward-single-

backscatter approximation. This assumes that the forward propagation can only scatter into the backward (reverberant) propagation direction once. Since energy initially only propagates outward, that is, only u_+ exists, it is reasonable that this will contribute to u_- .

This is seen in Eq. (2.18b) through the scattering term $\frac{\partial \mu}{\partial r} u_+$. With the single-backscatter approximation, we then say that the secondary scatter influence on u_+ by $\frac{\partial \mu}{\partial r} u_-$ in Eq. (2.18a) is negligible. Thus, the forward propagation is assumed to be unaffected by the small scale perturbations. The influence of μ is only to generate source terms for the backscattered field.

1. Forward Propagation

We can now obtain u_+ by defining $u_+ = \psi e^{ik_0 r}$ so that Eq. (2.18a) (ignoring the $\frac{\partial \mu}{\partial r} u_-$ term) becomes

$$\frac{\partial \psi}{\partial r} + ik_0 \hat{H}_{WAPE} \psi = 0, \quad (2.19)$$

which defines the evolution of the forward propagating PE field function ψ . The solution to this equation is obtained from the MMPE model with the long wavelength fluctuations built into \hat{n}^2 .

2. Backward Propagation

In similar fashion to the forward propagation problem, we define an incoming field function, $u_- = \Phi e^{-ik_0 r'}$, so that Eq. (2.18b) now becomes

$$\frac{\partial \Phi}{\partial r} \approx -ik_0 \Phi + \frac{1}{4\hat{n}} \frac{\partial \mu}{\partial r'} e^{ik_0 r'} \psi e^{ik_0 r}, \quad (2.20a)$$

noting that the second term on the right-hand side is the forward coupling term previously derived. The forward coupling term I , is identified as the inhomogeneous term in our solution for Φ ,

$$I = \frac{1}{4\hat{n}} \frac{\partial \mu}{\partial r'} \psi e^{ik_0(r'+r)}. \quad (2.20b)$$

Recall that ψ and Φ are the field functions of the two-way propagation with the long wavelength components built-in. The inhomogeneous term, I , then defines the coupling from scattering due to the short wavelength perturbations. In the next subsection, we will introduce the point source and then cast the incoming and outgoing fields into the form of the sonar equation and see the two-way coupling contributions likened to transmission losses but with a wave scattering strength.

3. Forcing Function

Up till now, we have only dealt with the homogeneous wave equation

$$\nabla^2 p + k^2 p = 0, \quad (2.21a)$$

with no hint of a source function. If a point source is now introduced, Eq. (2.21a) becomes

$$\nabla^2 p + k^2 p = -4\pi R_0 P_0 \delta(\vec{r} - \vec{r}_s), \quad (2.21b)$$

where P_0 is the source pressure at a reference distance R_0 . This may be expressed in terms of the Green's function, $g(\vec{r}, \vec{r}_s)$, which is the transfer function from a point source to a point receiver defined by (Jensen, et al., 1994)

$$(\nabla^2 + k^2)g(\vec{r}, \vec{r}_s) = -\delta(\vec{r} - \vec{r}_s), \quad (2.22a)$$

such that the pressure is

$$p(\vec{r}, \vec{r}_s) = 4\pi R_0 P_0 g(\vec{r}, \vec{r}_s). \quad (2.22b)$$

Extending this argument to an extended source, we can apply the idea of superposition of a number of point sources to say that

$$(\nabla^2 + k^2)p(\vec{r}) = f(\vec{r}) = -4\pi R_0 \int_{V_s} w(\vec{r}_s) \delta(\vec{r} - \vec{r}_s) d^3 r_s, \quad (2.23a)$$

then

$$p(\vec{r}_s) = 4\pi R_0 \int_{V_s} w(\vec{r}_s) g(\vec{r}, \vec{r}_s) d^3 r_s. \quad (2.23b)$$

We can also define the Green's function alternately in terms of the PE field function ψ by letting

$$4\pi R_0 g(\vec{r}, \vec{r}_s) = \sqrt{\frac{R_0}{r}} \psi(\vec{r}, \vec{r}_s) e^{ik_0 r}. \quad (2.24)$$

The corresponding inhomogeneous PE field function (Eq. (2.19)) for the *outward propagating field* due to a point source becomes

$$\frac{\partial \psi}{\partial r} + ik_0 \hat{H}_{WAVE} \psi = -4\pi \sqrt{\frac{r}{R_0}} e^{ik_0 r} \delta(\vec{r} - \vec{r}_s) \quad (2.25)$$

since $|\psi|=1$ is normalized at $r=R_0$. Similarly, the inhomogeneous form for the scattered (or backward propagating) field is

$$\frac{\partial \Phi}{\partial r} - ik_0 \hat{H}_{WAVE} \Phi = -4\pi \mathfrak{S}, \quad (2.26a)$$

where the inhomogeneous source term is due to the scattering of the forward propagating field, defined by

$$\mathfrak{S} = -\frac{1}{16\pi\hat{n}} \frac{\partial \mu}{\partial r'} \psi e^{ik_0(r+r')}, \quad (2.26b)$$

which acts like a point source function locally at the scattering point.

We now need to define some geometrical setup to aid in the understanding and development of the effects of scatter. Defining the location of the scattering point as \vec{r}_s and the volume of the scattering region as V_s , then the received scattered (backward propagating) field at location \vec{r}_R will be

$$p_-(\vec{r}_R) = 4\pi R_0 \int_{V_s} \mathfrak{S}(\vec{r}_s') \sqrt{\frac{R_0}{|\vec{r}_R - \vec{r}_s|}} e^{ik_0|\vec{r}_R - \vec{r}_s|} g(\vec{r}_R, \vec{r}_s) d^3 r_s. \quad (2.27)$$

Since the Green's function is the transfer function between two given points, we can say that $g(\vec{r}_R, \vec{r}_S)$ is the pressure field Green's function from each point within the scattering region to the point receiver location at \vec{r}_S . By reciprocity, we say that

$$g(\vec{r}_R, \vec{r}_S) = g(\vec{r}_S, \vec{r}_R). \quad (2.28a)$$

Also

$$g(\vec{r}_S, \vec{r}_R) = \frac{1}{4\pi R_0} p_+(\vec{r}_S, \vec{r}_R), \quad (2.28b)$$

then

$$\begin{aligned} p_-(\vec{r}_R) &= -\frac{1}{16\pi R_0} \int_{V_S} \frac{1}{\hat{n}} \frac{\partial \mu}{\partial r'} \sqrt{\frac{R_0}{|\vec{r}_S - \vec{r}_R|}} \psi(\vec{r}_S, \vec{r}_T) p_+(\vec{r}_S, \vec{r}_R) e^{ik_0|\vec{r}_T - \vec{r}_S|} d^3 r_S \\ &= -\frac{1}{16\pi R_0} \int_{V_S} \frac{1}{\hat{n}} \frac{\partial \mu}{\partial r'} p_{+T} p_{+R} d^3 r_S, \end{aligned} \quad (2.29)$$

where p_{+T} is the forward propagated field from the transmitter to the scattering point and p_{+R} is the forward propagated field from the receiver to the scattering point which by reciprocity is the same as p_{-R} .

We now examine the integrand term $\frac{1}{\hat{n}} \frac{\partial \mu}{\partial r'}$. Since \hat{n}^2 is defined in terms of the step function,

$$\hat{n}^2 = n_w^2(1 - H(z - \bar{z}_b - \eta_l)) + n_b^2 H(z - \bar{z}_b - \eta_l), \quad (2.30)$$

then with $H(0) = \frac{1}{2}$, the value of \hat{n}^2 at the interface is just the average value,

$$\hat{n}^2(z = z_b + \eta_l) = \frac{1}{2}(n_w^2 + n_b^2). \quad (2.31a)$$

Solving for \hat{n} gives

$$\frac{1}{\hat{n}} = \sqrt{\frac{2}{(n_w^2 + n_b^2)}}. \quad (2.31b)$$

Now

$$\frac{\partial \mu}{\partial r'} \approx (n_w^2 - n_b^2) \frac{\partial \eta_s}{\partial r'} \delta(z - \bar{z}_b - \eta_l), \quad (2.32)$$

where we have ignored the slower range variations in \bar{z}_b , η_l , n_w^2 and n_b^2 over the scattering region. Substituting the expressions in Eq. (2.31b) and (2.32) into Eq. (2.29), we obtain

$$\begin{aligned} p_-(\bar{r}_R) &\approx -\frac{1}{16\pi R_0} \int_{V_s} \sqrt{2} \frac{n_w^2 - n_b^2}{\sqrt{n_w^2 + n_b^2}} \frac{\partial \eta_s}{\partial r'} \delta(z - \bar{z}_b - \eta_l) p_{+T} p_{+R} d^3 r_s \\ &= -\frac{\sqrt{2}}{16\pi R_0} \frac{n_w^2 - n_b^2}{\sqrt{n_w^2 + n_b^2}} \int_{A_s} \frac{\partial \eta_s}{\partial r'} p_{+Tb} p_{+Rb} d^2 r_s, \end{aligned} \quad (2.33)$$

where p_{+Tb} and p_{+Rb} are the values evaluated at the bottom interface. Note that the range derivative of η_s is in the direction from the scattering patch to the receiver.

4. Statistical Treatment of the Scattered Field

Of interest is the mean squared reverberation from different roughness realizations, which from Eq. (2.33) is defined as

$$\langle |p_-|^2 \rangle = \frac{2}{(16\pi R_0)^2} \frac{(n_w^2 - n_b^2)^2}{n_w^2 + n_b^2} \iint \left\langle \left| \frac{\partial \eta_s}{\partial r} \frac{\partial \eta_s}{\partial r'} \right| p_{+Tb} p_{+Rb} p_{+Tb}^* p_{+Rb}^* \right\rangle d^2 r_s d^2 r'_s \quad (2.34)$$

where r_s and r'_s indicate two different boundary realizations. Consider the statistical characteristics of the roughness. We note that the small scale roughness must have zero mean, i.e. $\langle \eta_s \rangle = 0$ and has an amplitude spectrum of $S_{\eta_s, 2D}(K, L)$ for a given realization, such that

$$\eta_s(x, y) = \iint S_{\eta_s, 2D}(K, L) e^{iKx} e^{iLy} dK dL, \quad (2.35)$$

where K and L are the horizontal wavenumbers in the x - and y -directions, respectively. Here, the amplitude spectrum, $S_{\eta_s, 2D}(K, L)$, refers to the 2-D roughness of only the small-scale perturbations, therefore the subscripts ' $\eta_s, 2D$ '. The rms roughness is then given by

$$\langle |\eta_s|^2 \rangle = \iint dK dL \iint dK' dL' S_{\eta_s, 2D}(K, L) S_{\eta_s, 2D}^*(K', L') e^{i(K-K')x} e^{i(L-L')y} . \quad (2.36)$$

Assuming a wide-sense-stationary spectrum in space, then

$$\langle |\eta_s|^2 \rangle = \iint dK dL W_{\eta_s, 2D}(K, L) , \quad (2.37)$$

where $W_{\eta_s, 2D}(K, L) = |S_{\eta_s, 2D}(K, L)|^2$ is the power spectrum. The spatial correlation function for the roughness can then be defined as

$$\langle \eta_s(x, y) \eta_s(x - x', y - y') \rangle = \iint dK dL W_{\eta_s, 2D}(K, L) e^{iK(x-x')} e^{iL(y-y')} . \quad (2.38)$$

Hence for a given realization,

$$\left\langle \frac{\partial \eta_s}{\partial r} \frac{\partial \eta_s}{\partial r} \right\rangle = \iint k_r^2 W_{\eta_s, 2D} e^{iK(x-x')} e^{iL(y-y')} dK dL , \quad (2.39a)$$

where

$$k_r = K \cos \phi , \quad (2.39b)$$

and ϕ is angle in the direction of r towards the receiver relative to the (x, y) coordinate system. The following diagram shows the geometry being developed here.

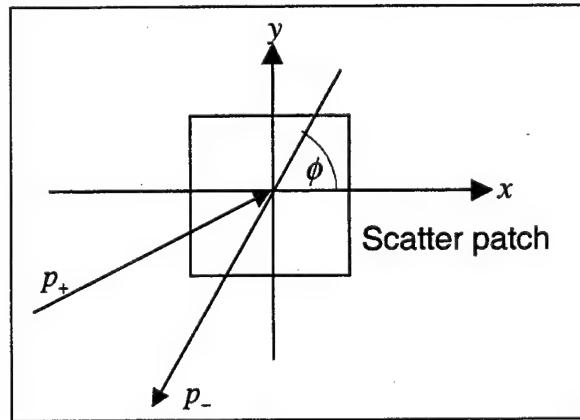


Figure 2.1 - Scatter Geometry

Conversely, the alternate-domain realization may be expressed as,

$$\iint \left\langle \left| \frac{\partial \eta_s(x, y)}{\partial r} \frac{\partial \eta_s(x-x', y-y')}{\partial r} \right| \right\rangle e^{-ik(x-x')} e^{-iL(y-y')} d(x-x') d(y-y') \quad (2.39c)$$

$$= k_r^2 W_{\eta_s, 2D}(K, L).$$

The above equations may be considered as the transform pairs for achieving a bottom realization.

Let us now set up a spatial representation of the notations that will be used in the ensuing arguments. Consider two scatter points, r_s and r'_s located at their respective distances from the transmitter, T , and the receiver, R . These are shown in the following diagram.

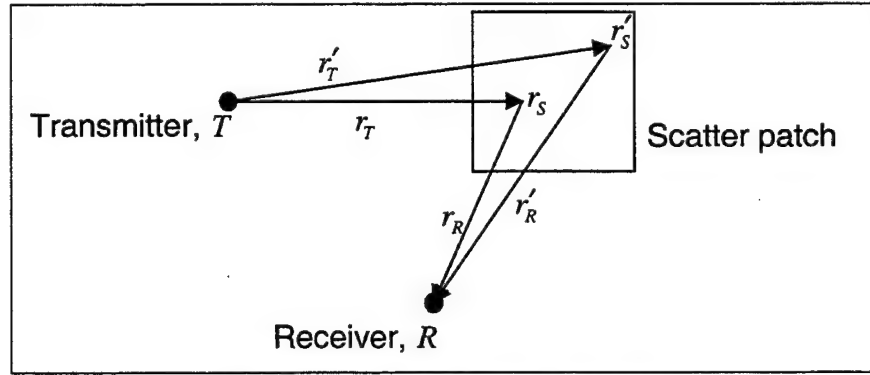


Figure 2.2 - 2-Point Scatter Geometry

The backward propagation or scattered field in Eq. (2.34) may now be written as

$$\langle |p_-|^2 \rangle = B \iint \left\langle \left| \frac{\partial \eta_s(x, y)}{\partial r_R} \frac{\partial \eta_s(x', y')}{\partial r'_R} \right| \right\rangle \frac{1}{\sqrt{r_T r_R}} \frac{1}{\sqrt{r'_T r'_R}} \psi_{Tb}(r_T) \psi_{Rb}(r_R) \psi_{Tb}^*(r'_T) \psi_{Rb}^*(r'_R) \quad (2.40a)$$

$$\times e^{ik_0(r_T + r_R - r'_T - r'_R)} d^2 r_s d^2 r'_s$$

where

$$B = \frac{2}{(16\pi R_0)^2} \frac{(n_w^2 - n_b^2)^2}{n_w^2 + n_b^2}. \quad (2.40b)$$

We have thus far assumed that the fields vary slowly in range, and over a given scattering patch the $\frac{1}{\sqrt{r_T r_R}}$ amplitude terms also vary slowly. Furthermore, since η_s and $\frac{\partial \eta_s}{\partial r}$ decorrelate rapidly for $r_T \neq r'_T$ and $r_R \neq r'_R$, then we may assume that these are the same in the amplitude terms and the locations of evaluation. Hence, the field functions become independent of the integral over the scattering patch so that

$$\begin{aligned} \langle |p_-|^2 \rangle &\approx \frac{B}{\bar{r}_T \bar{r}_R} \langle |\psi_{Tb}(\bar{r}_T)|^2 |\psi_{Rb}(\bar{r}_R)|^2 \rangle \times \\ &\iint \left\langle \left| \frac{\partial \eta_s(x, y)}{\partial r_R} \frac{\partial \eta_s(x', y')}{\partial r_R} \right| e^{ik_0(r_T + r_R - r'_T - r'_R)} \right\rangle d^2 r_s d^2 r'_s \end{aligned} \quad (2.41)$$

where $\bar{r}_T = \frac{1}{2}(r_T + r'_T)$, $\bar{r}_R = \frac{1}{2}(r_R + r'_R)$ are the mean values of the distances from the scattering patch to the receiver and transmitter.

Introducing *difference* variables, $r''_T = r'_T - r_T$ and $r''_R = r'_R - r_R$, and assuming the roughness is isotropic, $W_{\eta_s, 2D}(K, L) = W_{\eta_s, 2D}(k)$, we can write the above integral as

$$\iint \left\langle \left| \frac{\partial \eta_s(x, y)}{\partial r_R} \frac{\partial \eta_s(x - x'', y - y'')}{\partial r_R} \right| \right\rangle e^{-ik_0(r''_T + r''_R)} d^2 r_s d^2 r''_s = \int k_r^2 W_{\eta_s, 2D}(k) d^2 r_s \quad (2.42)$$

where $k = k_0^2 [(\cos \phi_T + \cos \phi_R)^2 + (\sin \phi_T + \sin \phi_R)^2]$. We now assume that over the small scattering patch, k_r^2 and $W_{\eta_s, 2D}(k)$ vary slowly so that

$$\langle |p_-|^2 \rangle \approx \frac{B}{\bar{r}_T \bar{r}_R} |\psi_{Tb}(\bar{r}_T)|^2 |\psi_{Rb}(\bar{r}_R)|^2 k_r^2 W_{\eta_s, 2D}(k) \Delta A_b, \quad (2.43)$$

and ΔA_b is the area of the scattering patch on the bottom interface. The new geometry based on the mean distances from the scattering patch is shown in the following figure.

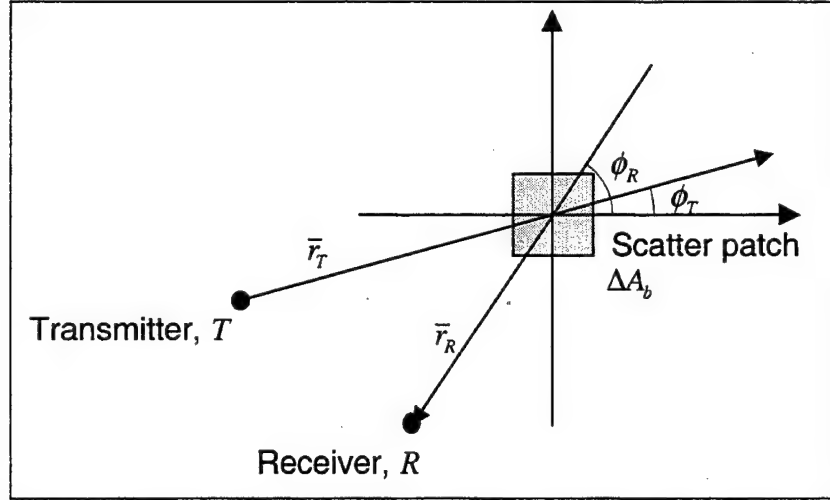


Figure 2.3 – Scatter Geometry Based on Mean Distances from Scatter Patch

To simplify the analysis, we realign the diagram to have the receiver line coincide with the x -axis, i.e. $\phi_R = 0$. Then $k_r = k = k_0 \cos \phi_T$ and $k = 2k_0 \cos \frac{\phi_T}{2}$. Note that this wavenumber indicates that the spectrum is evaluated at the Bragg wavenumber. The following figure shows the re-oriented scatter geometry.

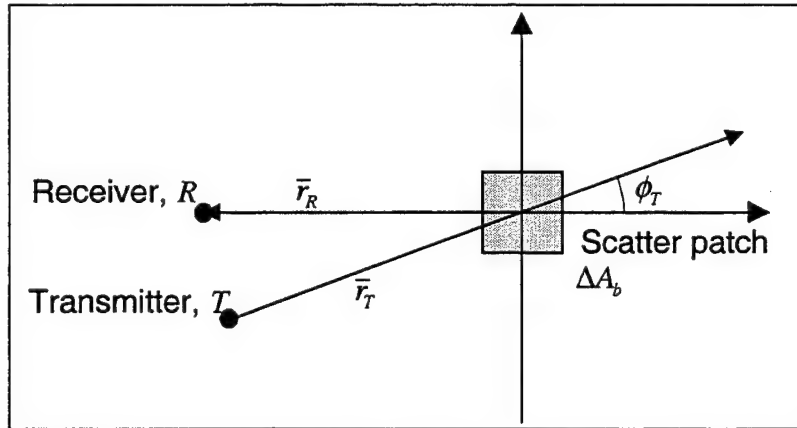


Figure 2.4 – Re-Oriented Geometry for $\phi_R = 0$

For monostatic scatter then, we have

$$\langle |p_-|^2 \rangle = \frac{2k_0^2}{(16\pi R_0)^2} \frac{(n_w^2 - n_b^2)^2}{n_w^2 + n_b^2} \langle |\psi_b|^4 \rangle W_{\eta_s, 2D}(2k_0) \Delta A_b \quad (2.44)$$

where $r = \bar{r}_T = \bar{r}_R$ and $|\psi_b| = |\psi_{Tb}| = |\psi_{Rb}|$. Now writing $n_b = n_w + \Delta n = n_w \left(1 + \frac{\Delta n}{n_w}\right)$

$= n_w(1 + \delta)$ where $\delta \ll 1$, then

$$\begin{aligned} \frac{(n_w^2 - n_b^2)^2}{n_w^2 + n_b^2} &= n_w^2 \frac{(1 - (1 + \delta)^2)^2}{1 + (1 + \delta)^2} \approx n_w^2 \frac{(1 - (1 + 2\delta))^2}{1 + (1 + 2\delta)} \\ &= n_w^2 \frac{(-2\delta)^2}{2(1 + \delta)} \approx 2n_w^2 \delta^2 (1 - \delta) \approx 2n_w^2 \delta^2 = 2(\Delta n)^2. \end{aligned} \quad (2.45a)$$

Furthermore, $\Delta n = n_b - n_w = \frac{c_0}{c_b} - \frac{c_0}{c_w} = \frac{c_0(c_w - c_b)}{c_w c_b} = \frac{c_0 \Delta c}{c_w c_b}$, so

$$(\Delta n)^2 = \frac{c_0^2}{c_w^2 c_b^2} (\Delta c)^2 \approx \left(\frac{\Delta c}{c_0}\right)^2, \text{ since } c_w \sim c_b \sim c_0. \quad (2.45b)$$

Finally for the monostatic case, the backscatter field becomes

$$\langle |p_-|^2 \rangle = \frac{k_0^2}{(8\pi r R_0)^2} \left(\frac{\Delta c}{c_0}\right)^2 \langle |\psi_b|^4 \rangle W_{\eta_s, 2D}(2k_0) \Delta A_b. \quad (2.46)$$

5. Mean Squared Reverberation Pressure Level, RPL

Of interest is the mean squared reverberation pressure level, RPL. Reciprocity of the one-way fields has been invoked in order to write the solution in terms of the outgoing field. Using the solution for the incoming field in Eq. (2.46), we can now cast this into the form of a SONAR equation. We do this by considering the contributions of the source level, directional characteristics of the source and receiver and the area of ensonification being captured in that region of the beams. Hence assuming that the field functions do not vary rapidly over the scattering region and the spectrum of the roughness is isotropic, the monostatic reverberation pressure level can be expressed as

$$RPL = 10 \log \left(\left\langle \frac{|p_-|^2}{p_{ref}^2} \right\rangle \right) = SL + DI_T + DI_R + 10 \log \left(\frac{\Delta A_b}{R_0^2} \right) - RL_{b,v}, \quad (2.47)$$

where SL is the source level, $DI_{T/R}$ are the directivity index for the transmitter/receiver respectively, and ΔA_b is the ensonified area of the bottom interface scattering. The reverberation loss has also been correspondingly defined as a general function of either the boundary or the volume. This reverberation loss analysis applied to the boundary, from the analysis in the previous section, is defined by

$$\begin{aligned} RL_b &= -10 \log \left[\frac{k_0^2}{(8\pi r)^2} \left(\frac{\Delta c}{c_0} \right)^2 \langle |\psi_b|^4 \rangle W_{\eta_s, 2D}(2k_0) \right] \\ &= -10 \log \left[\frac{1}{r^2} \langle |\psi_b|^4 \rangle \right] - 10 \log \left[\frac{k_0^2}{(8\pi)^2} \left(\frac{\Delta c}{c_0} \right)^2 W_{\eta_s, 2D}(2k_0) \right]. \end{aligned} \quad (2.48a)$$

If the field has fully saturated statistics, which is often true, then

$$\langle |\psi_b|^4 \rangle = 2 \langle |\psi_b|^2 \rangle^2. \quad (2.48b)$$

Then,

$$\begin{aligned} RL_b &= -20 \log \left[\frac{1}{r} \langle |\psi_b|^2 \rangle \right] - 10 \log \left[\frac{k_0^2}{(8\pi)^2} \left(\frac{\Delta c}{c_0} \right)^2 W_{\eta_s, 2D}(2k_0) \right] \\ &= 2TL_b - 10 \log \left[\frac{k_0^2}{32\pi^2} \left(\frac{\Delta c}{c_0} \right)^2 W_{\eta_s, 2D}(2k_0) \right], \end{aligned} \quad (2.49)$$

where TL_b is the transmission loss from monostatic source/receiver to the scattering patch at the bottom. Finally, we can write,

$$RL_b = 2TL_b - S_b, \quad S_b = 10 \log \left[\frac{k_0^2}{32\pi^2} \left(\frac{\Delta c}{c_0} \right)^2 W_{\eta_s, 2D}(2k_0) \right], \quad (2.50)$$

where S_b is the full-wave scattering strength due to the small-scale interface roughness, and $W_{\eta_s, 2D}(2k_0)$ is the 2-D spectrum of the interface roughness evaluated at the Bragg wavenumber.

One should note the following points:

- If the statistics of the interface are homogeneous over a large portion of the area of interest, the interface reverberation structure is controlled by two-way transmission loss.
- Because the two-way transmission loss is dominated by forward and backward propagation over long-wavelength features, the statistics of this signal should be related to the low spatial wavenumber-space statistics.

The statistical model to be used for the interface roughness will be treated in the next chapter.

B. VOLUME SCATTERING

Having trudged through the analysis of the bottom interface extensively, the volume scattering development will take on the same general form with the exception that the index of refraction varies three-dimensionally in space. We will specifically consider for now only the theoretical development of sound speed variations and the overall effects on scattering and reverberation. The other element affecting volume scattering is density variations in the volume, which will not be treated in this thesis but will be left for follow-on work.

We start with the wave equation in Eq. (2.1) and the index of refraction perturbations in the spatial scale in Eq. (2.3),

$$\nabla^2 p + k_0^2 n^2 p = 0, \quad (2.51)$$

and

$$n^2 = n_w^2(1 - H(z - z_b)) + n_b^2 H(z - z_b), \quad (2.52)$$

as before, but now the bottom (volume) index of refraction varies three-dimensionally in space, $n_b(x, y, z)$. As before in the statistical treatment of the interface spatial variation, sound speed variations may be defined by (Yamamoto, 1995)

$$c_b(x, y, z) = c_{b0}(1 + bz + \delta(x, y, z)), \quad (2.53)$$

where c_{b0} is the mean bottom sound speed at the interface, $b = \frac{g}{c_{b0}}$ is the normalized gradient of the bottom sound speed, and δ is the zero-mean random perturbation, i.e. $\langle \delta \rangle = 0$ and

$$\langle \delta(x, y, z), \delta(x', y', z') \rangle = \iiint W_{\delta,3D}(K, L, M) e^{iK(x-x')} e^{iL(y-y')} e^{iM(z-z')} dK dL dM, \quad (2.54)$$

where $W_{\delta,3D}(K, L, M)$ represents the 3-D power spectrum of the fluctuations.

Again we break this up into long and short wavelength components by having the random perturbations split as

$$\delta = \delta_l + \delta_s, \quad (2.55)$$

such that Eq. (2.53) now becomes

$$\begin{aligned} c_b(x, y, z) &= c_{b0}(1 + bz + \delta_l) + c_{b0}\delta_s \\ &= \bar{c}_b(x, y, z) + c_{b0}\delta_s(x, y, z). \end{aligned} \quad (2.56)$$

This can be incorporated into the index of refraction by writing

$$\begin{aligned} n_b^2 &= \left(\frac{c_0}{c_b} \right)^2 = \frac{c_0^2}{c_{b0}^2(1 + bz + \delta_l + \delta_s)^2} \\ &\approx \frac{c_0^2}{\bar{c}_b^2} (1 - 2\delta_s) = \hat{n}_b^2 + \mu_b, \end{aligned} \quad (2.57a)$$

where now

$$\mu_b = -2\hat{n}_b^2\delta_s \quad (2.57b)$$

and \hat{n}_b^2 is, as before, the description of the environment including all long wavelength component perturbations.

The general description of the environment of Eq. (2.52) is now

$$\hat{n}^2 = n_w^2(1 - H(z - \bar{z}_b - \eta_l)) + \hat{n}_b^2 H(z - \bar{z}_b - \eta_l), \quad (2.58)$$

and the effects of interface scatter and volume scatter may be considered separately. Note that the long-wavelength contribution to the interface roughness has been included as η_l into the perturbation, which in turn affects the effective index of refraction. The derivation now follows exactly as before arriving at the final result for the bottom interface in Eq. (2.33),

$$p_- = -\frac{1}{16\pi R_0} \int_{V_s} \frac{1}{\hat{n}} \frac{\partial \mu_b}{\partial r} p_{+T} p_{+R} d^3 r_s, \quad (2.59)$$

where the volume integration occurs over the sediment volume scattering region, i.e. $z > \bar{z}_b + \eta_l$.

We now have

$$\frac{\partial \mu_b}{\partial r} \approx -2\hat{n}^2 \frac{\partial \delta_s}{\partial r}, \quad (2.60)$$

which remains a volumetric quantity, so

$$p_- = \frac{2}{16\pi R_0} \int_{V_s} \hat{n} \frac{\partial \delta_s}{\partial r} p_{+T} p_{+R} d^3 r_s. \quad (2.61)$$

Taking the same approach as the interface in Eq. (2.34), we see that the mean squared volume reverberation is then

$$\begin{aligned} \langle |p_-|^2 \rangle &= \frac{1}{(8\pi R_0)^2} \iint \langle \hat{n}(r_s) \hat{n}(r'_s) \frac{\partial \delta_s(x, y, z)}{\partial r} \frac{\partial \delta_s(x', y', z')}{\partial r} \times \\ &\quad p_{+Tb} p_{+Rb} p_{+Tb}^* p_{+Rb}^* \rangle d^3 r_s d^3 r'_s. \end{aligned} \quad (2.62)$$

As before, we write the pressure fields in terms of the field function, ψ (see Eq. (2.40a)), and argue that they do not change significantly in range within the scattering region. They do, however, vary considerably in depth, so

$$\begin{aligned} \langle |p_-|^2 \rangle &= \frac{1}{(8\pi R_0)^2} \frac{1}{\bar{r}_T} \frac{1}{\bar{r}_R} \iint_{zz'} \langle \psi_T(\bar{r}_T, z) \psi_T^*(\bar{r}_T, z') \psi_R(\bar{r}_R, z) \psi_R^*(\bar{r}_R, z') \hat{n}(r_s) \hat{n}(r'_s) \rangle \\ &\quad \times \iint_{xyx'y'} \left\langle \frac{\partial \delta_s}{\partial r}(x, y, z) \frac{\partial \delta_s}{\partial r}(x', y', z') \right| e^{ik_0(r_T + r_R - r'_T - r'_R)} \rangle d^2 r_s d^2 r'_s dz dz' \end{aligned} \quad (2.63a)$$

Recall that $\bar{r}_T = \frac{1}{2}(r_T + r'_T)$ and $\bar{r}_R = \frac{1}{2}(r_R + r'_R)$. The inner term is evaluated over difference variables (as before in Eq. (2.42)) r''_T and r''_R to give

$$\iint_{xy,xy'} \left\langle \frac{\partial \delta_s}{\partial r}(x, y, z) \frac{\partial \delta_s}{\partial r}(x - x'', y - y'', z - z'') \right\rangle e^{-ik_0(r''_T + r''_R)} d^2 r_s d^2 r''_s \quad (2.63b)$$

$$\approx \int k_r^2 W_{\delta_s, 2D_H}(K'', L'') d^2 r_s$$

where K'' , L'' and k_r are as before, but

$$W_{\delta_s, 2D_H}(K, L) \equiv W'_{\delta_s, 3D}(K, L, z - z') = \int W_{\delta_s, 3D}(K, L, M) e^{iM(z - z')} dM \quad (2.63c)$$

is the 2D spectrum of the small scale perturbations in the horizontal dimension.

If we now assume that the spectral density is essentially a delta-correlated function in depth and horizontally isotropic, then we can say that $W_{\delta_s, 2D_H}(K, L) = W_{\delta_s, 2D_H}(k) = W'_{\delta_s, 3D}(k, 0) \delta(z - z')$, and neglect variations in $W_{\delta_s, 2D_H}$ over the scattering region. Then, assuming a monostatic geometry,

$$\begin{aligned} \langle |p_-|^2 \rangle &= \frac{1}{(8\pi R_0)^2} \frac{1}{r^2} \int_{z_b + \eta_l}^{\infty} \langle \hat{n}^2(r, z) |\psi_T(r, z)|^2 |\psi_R(r, z)|^2 \rangle \\ &\quad \times k_r^2 W_{\delta_s, 2D_H}(k) dz \Delta A, \end{aligned} \quad (2.64)$$

ΔA being the horizontal area extent of the scattering volume, much akin to the scattering patch for the interface reverberation development.

For backscatter then,

$$\begin{aligned} \langle |p_-|^2 \rangle &= \frac{1}{(8\pi R_0)^2} \frac{1}{r^2} \int_{z_b + \eta_l}^{\infty} \langle \hat{n}^2(r, z) |\psi_T(r, z)|^2 |\psi_R(r, z)|^2 \rangle \\ &\quad \times k_0^2 W_{\delta_s, 2D_H}(2k_0) dz \Delta A. \end{aligned} \quad (2.65a)$$

If we now assume that the spectrum $W_{\delta_s, 2D_H}$ does not change significantly with depth, then

$$\langle |p_-|^2 \rangle \approx \left(\frac{k_0}{8\pi r R_0} \right)^2 W_{\delta_s, 2D_H} (2k_0) \Delta A \int_{z_b + \eta_l}^{\infty} \langle \hat{n}^2(r, z) |\psi(r, z)|^4 \rangle dz. \quad (2.65b)$$

Finally, we will assume that $\langle \hat{n}^2(r, z) |\psi(r, z)|^4 \rangle \approx 2 \langle \hat{n}(r, z) |\psi(r, z)|^2 \rangle^2$, similar to our previous treatment of fully saturated statistics.

For the volume reverberation problem, we see that we cannot write the RPL simply in terms of transmission loss (TL) but instead must integrate over depth the quantity $\langle \hat{n}(r, z) |\psi(r, z)|^2 \rangle^2$ at each range, r . We shall then use a form of ergodicity and write

$$\int \langle \hat{n}(r, z) |\psi(r, z)|^2 \rangle^2 dz \approx \left\langle \int \hat{n}(r, z) |\psi(r, z)|^2 dz \right\rangle^2, \quad (2.65c)$$

and since \hat{n} and ψ are based only on the long wavelength components, we will simply say that we can use $\left(\int \hat{n}(r, z) |\psi(r, z)|^2 dz \right)^2$. Then as in Eq. (2.47), we may write

$$RPL = 10 \log \left(\left\langle \frac{|p_-|^2}{P_{ref}^2} \right\rangle \right) = SL + DI_T + DI_R + 10 \log \left(\frac{\Delta A_b}{R_0^2} \right) - RL_v, \quad (2.66a)$$

where

$$RL_v = -20 \log \left[\frac{1}{r} \int_{z > z_b + \eta_l}^{\infty} \hat{n}(r, z) |\psi(r, z)|^2 dz \right] - 10 \log \left[\frac{k_0^2}{32\pi^2} W_{\delta_s, 2D_H} (2k_0) \right]. \quad (2.66b)$$

In the above expression, $W_{\delta_s, 2D_H} (2k_0)$ is the 2-D horizontal spectrum of the volume fluctuations, which is assumed isotropic and independent of depth (as in the interface reverberation problem) evaluated at the Bragg wavenumber, and the depth integral extends from the bottom interface downwards to negative infinity. Note that volume reverberation loss cannot be expressed simply in terms of the two-way transmission loss as before.

One should also note the following few points:

- The reverberation loss is not independently influenced by the forward propagating fields, but is a magnitude scaling or weighting function of the local index of refraction (positive definite).
- If the statistics of the volume are homogeneous over a large portion of the area of interest, the volume reverberation structure is controlled by this non-linear, two-way transmission loss between sound speed structure and acoustic field.
- Because this weighted two-way transmission loss is dominated by forward and reciprocal propagation over long-wavelength features, the statistics of this signal should be related to the low spatial wavenumber-space statistics, as in the case of interface reverberation. We will however expect to see smoother changes (not abrupt) as compared to the interface reverberation statistics. This is because the statistics apply non-linearly here providing only the mean-square positive-definite weighted average of the acoustic interactions with the environment.

The statistical model to be used for the volume sound speed variations will be treated in Chapter III.

C. TIME-DOMAIN ANALYSIS

1. Time-Domain Analysis of the Interface

Up until now, the focus has been on CW analysis. The previous analyses for both the interface and volume have suggested that the structure of the reverberation is due mainly to the effects of propagation. To predict the effects of a pulsed signal instead of the CW signal, the MMPE/MMPEREV model is run over a spectrum of frequencies. Subsequently, Fourier analysis will give the time-domain structure of the pulse propagation in time.

In shallow water, propagation of a signal from a point source will experience multipath effects. In the time-domain, a scatter patch receiving multipath arrivals will scatter the received signal at different arrival times. The scattering patch, by reciprocity, scatters the entire received signal back through the same multipaths (monostatic geometry assumed) that each signal has traversed, leading to the receiver receiving multiple-multipath signals at different times. Thus, the scattering patch is a source, producing time-delayed replicas (with proper amplitude weightings) back to the receiver through the multipath structure of the water column. The geometry of the development may be represented by the following diagram.

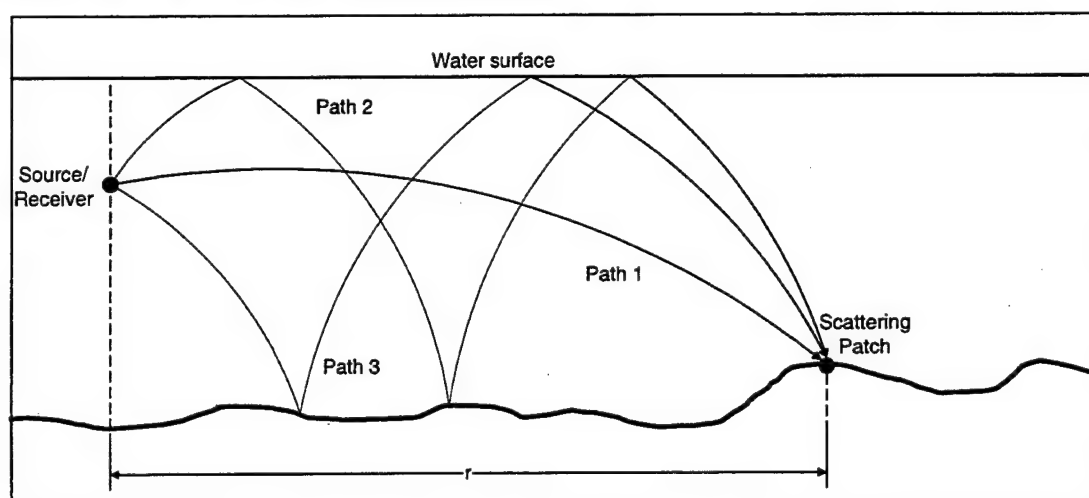


Figure 2.5 –Two-way return from a single scattering point

As the source transmits a signal out to the scattering patch, the scattering patch receives signals along all the multipaths (in the figure above, just three multipaths). The scattering patch scatters each signal and, by reciprocity, these scattered signals follow the same (three) multipaths back to the source location. Recall that the Green's function is the transfer function between the source and the receiver and it does not matter which direction the propagating wave is travelling. Hence, from a signal point of view, these may be represented as depicted in Figure 2.6. The total reverberation signal from this scattering patch would then be the coherent sum of the three lower panels.

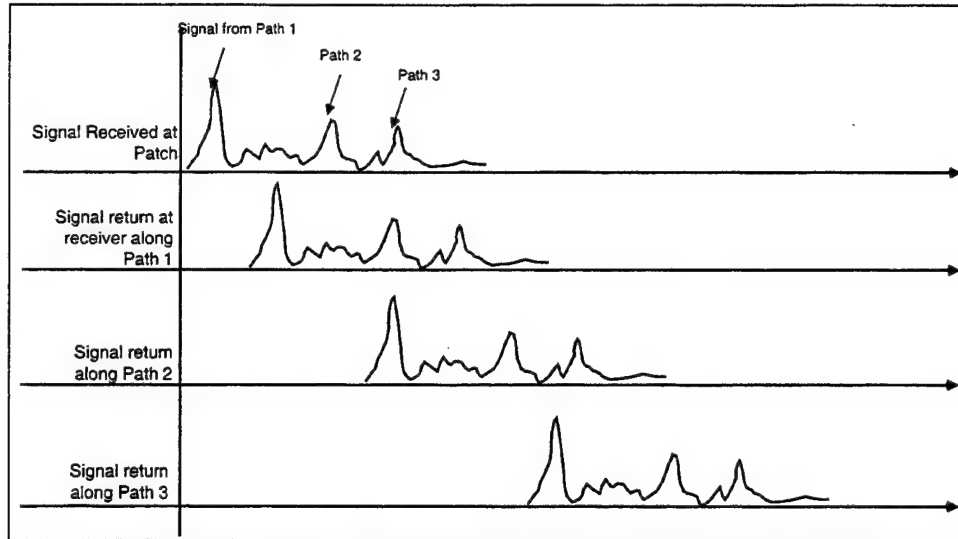


Figure 2.6 – Signal At Receiver Due to Multipath Reverberation

In general, if the receiver and source are not co-located, it may be useful to consider the arrival times of the same signal from the source and receiver to the same scatter point/patch. By reciprocity, we may say that the receiver has “propagated” the signal towards the scatter patch. The geometry has been adapted from Smith and Cushman (1997) as shown, in Figure 2.7.

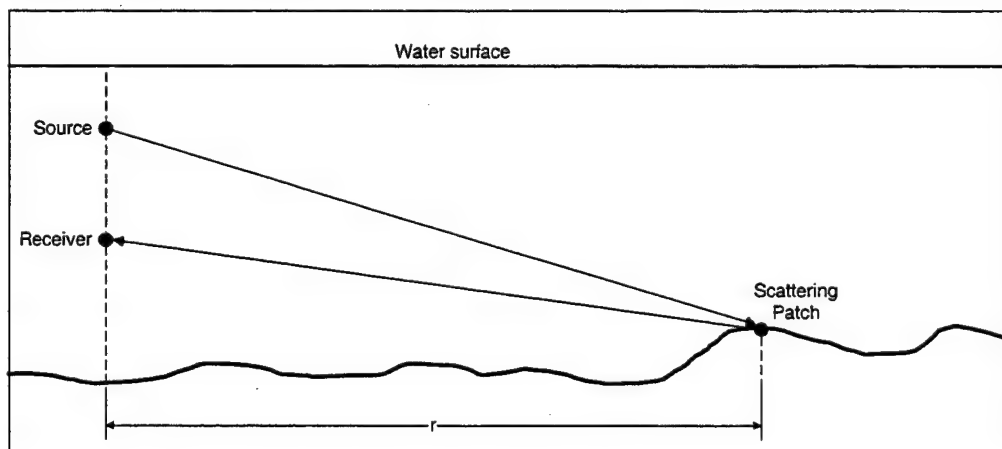


Figure 2.7 – Two-way return from a Scattering Patch

These two propagations may be considered independent and in order to compute the total reverberant field at the receiver, we may convolve the two field functions as explained by Smith and Cushman (1997). With an understanding of the pulsed propagation and

multipaths, the one-way time-domain pressure due to a pulsed signal at the scattering patch is

$$p_{+T/Rb}(r_m, t) = \int \left[\frac{1}{\sqrt{r_m}} \psi_{T/Rb}(r_m, f) e^{i \frac{2\pi f}{c_0} r_m} \right] e^{-i 2\pi f t} df, \quad (2.67)$$

where the forward propagated pressure field from the transmitter/receiver at the interface, $p_{+T/Rb}$, is specified at range r_m , which is the range at the m^{th} range step. The field-function evaluated at the interface at range r_m and at frequency f may be extracted from the forward propagation of the broadband field computed by MMPE. Notice that in order to arrive at the required pressure in the time domain, we have to integrate over all the frequencies, and the above expression is really the Fourier transform of the field in the frequency domain.

Extending the argument further, the travel time of the two-way pressure field at the receiver is now the convolution (Smith and Cushman, 1997) of two, one-way fields in the time-domain propagated forward. This is

$$p_{2-way,b}(r_m, \tau) = \int p_{+Tb}(r_m, t) p_{+Rb}(r_m, \tau - t) dt, \quad (2.68a)$$

where we recall from Eq. (2.33) that p_{+Tb} and p_{+Rb} are the forward propagated fields from the transmitter and receiver to the scattering point evaluated at the bottom interface, respectively. Note that the forward propagated field from the receiver to the scattering point is by reciprocity the same as p_{-Rb} . We also note that the transmitter and receiver need not be co-located in depth.

Applying the above approach, we see that the time-convolution of the two field functions is also the frequency multiplication of these functions in the frequency domain. Hence, when the forward propagating fields are already available in the frequency domain, we may then compute the two-way field in the frequency domain from the interface as

$$p_{2-way,b}(r_m, f) = p_{+Tb}(r_m, f) p_{+Rb}(r_m, f), \quad (2.68b)$$

where

$$p_{+Tb}(r_m, f) = \frac{1}{\sqrt{r_m}} \psi_{+Tb}(r_m, f) e^{ik_0 r}, \text{ and} \quad (2.68c)$$

$$p_{+Rb}(r_m, f) = \frac{1}{\sqrt{r_m}} \psi_{+Rb}(r_m, f) e^{ik_0 r},$$

at a particular bottom depth, $z_b(r_m)$, at range r_m , and at each frequency. By applying Eq. (2.67), we can then arrive at the two-way travel time structure of the reverberation loss (RL_b) due to a single bottom patch, i.e.

$$p_-(r_m, t) = A \int p_{2\text{-way}, b}(r_m, f) e^{-i2\pi f t} df, \quad (2.68d)$$

where the constant A has been included to incorporate all the other factors needed to define reverberation loss.

We then continue our propagation through the entire water space of interest and arrive at the reverberant field at each range step. To see the total field at the receiver, we coherently sum up all the pressure values from different range segments, r_m , by matching up the discrete arrival times, t_n ,

$$p_-(t_n) = \sum_{m=1}^M p_-(r_m, t_n) \quad (2.69)$$

where p_- is the total pressure at the receiver received at time t_n . Note that this matching requires a coordinated scaling between range step size and time step size, as will be explained in Chapter IV.

2. Time-Domain Analysis of the Volume

The volume analysis is a 2-D problem in that the reverberation is not directly proportional to the two-way transmission loss, but requires proper weights through the entire volume when computing the reverberant field at the receiver. The development will follow closely that of the previous sub-section on the interface.

Firstly, the reverberant field due to each depth/range point is computed using the frequency-multiplication of the source-patch and patch-receiver (by reciprocity, the

forward propagation used) propagating fields, and then applying a Fourier transform to the time-domain. This is

$$p_{2\text{-way}}(r_m, z, f) = n(r_m, z) p_{+T}(r_m, z, f) p_{+R}(r_m, z, f), \quad (2.70a)$$

where now the two-way reverberation signal is computed for every grid point of interest ($z > z_b$ always) at a particular frequency, f , and $n(r_m, z)$ is the local index of refraction at the grid point. The justification for multiplying by the local index of refraction is to provide the same weighting used in the CW analysis. Fourier transforming gives

$$p_{2\text{-way}}(r_m, z, t) = \int p_{2\text{-way}}(r_m, z, f) e^{-i2\pi ft} df. \quad (2.70b)$$

The 2-D problem may now be reduced to a 1-D problem by performing a vertical integration to arrive at a single reverberation time-series, i.e.

$$p_-(r_m, t) = B \int_{z>z_b}^{\infty} p_{2\text{-way}}(r_m, t) dz, \quad (2.71)$$

which is the coherent sum over all depths below the interface at range step m . Note that the constant B has been introduced to account for all remaining terms in the reverberation loss, RL_v . We have now 'collapsed' the volume in 2-D to 1-D, giving a single set of time-series which can then be matched and summed,

$$p_-(t_n) = \sum_{m=1}^M p_-(r_m, t_n), \quad (2.72)$$

giving a single time-series in $p_-(t_n)$ which is the two-way time-domain field defining the volume reverberation loss at the receiver at time t_n due to the entire volume in the space of interest.

In the post-processing analysis to be discussed in Chapter IV, we will implement the above discussions for both the interface and volume to arrive at the time-domain analysis.

THIS PAGE IS INTENTIONALLY LEFT BLANK

III. GENERATING REALIZATIONS – IMPLEMENTATION OF THE REVERBERATION PROBLEM IN MMPE

Having developed the theoretical basis for modeling the interface and bottom variabilities, we now have to define statistical methods or models to generate the interface and sound speed variations. We first developed the theoretical aspects of the models used for generating both the interface and volume perturbations, then implemented the algorithms in MATLAB to enable checking of the theoretical developments before integrating them as functions into the MMPE model (Smith, 2000) written in FORTRAN 95. Much of the theoretical development for generating perturbations to the interface is based on the work of Goff and Jordon (1988) while the model for the volume is based on Yamamoto's (1995) work.

We should note that generating good realizations would form an important first step in the effort to model shallow water reverberation and their effects on sound propagation. Of particular importance are the "tweaking" that must be afforded in root-mean-square values when generating these realizations so that we are able to study the effects of different bottom undulations and sediment types.

A. SPECTRAL DESCRIPTIONS OF BOTTOM VARIABILITY

1. Interface Roughness (Spatial Perturbation)

From Chapter II, we have seen that the interface effects can be separated into both long- and short-wavelength fluctuations. We have principally neglected the short wavelength components in the forward propagation problem. Since the interface roughness is essentially 2-D, we can assume a 2-D interface spectrum of the form

$$W_{\eta_s, 2D}(k_r) = \frac{\mu}{(1 + L_{corr}^2 k_r^2)^{\beta_\eta/2}}, \quad k_r = \sqrt{K^2 + L^2}, \quad (3.1)$$

where L_{corr} is a correlation length scale, β_η is a spectral exponent, and k_r is the horizontal spatial wavenumber vector. Note that for $k_r \gg 1/L_{corr}$,

$$W_{\eta_s, 2D}(k_r \gg L_{corr}) \sim k_r^{-\beta_\eta}. \quad (3.2)$$

The normalization factor μ is defined in terms of the root-mean-square (rms) roughness σ^2 by requiring

$$2\pi \int_0^\infty W_{\eta_s, 2D}(k_r) k_r dk_r = \sigma^2, \quad (3.3)$$

which leads to

$$\mu = \frac{1}{\pi} \left(\frac{\beta_\eta}{2} - 1 \right) \sigma^2 L_{corr}^2. \quad (3.4a)$$

Note that k_r is the horizontal component of the wavenumber, and the 2-D spectrum, $W_{\eta_s, 2D}$, is assumed isotropic (independent of direction).

For this description, the exponent β_η is constrained by

$$2 < \beta_\eta < 4. \quad (3.4b)$$

Consistent with previous reverberation work by Goff & Jordan (1988) on a rough interface, we shall assume a fractal character with $\beta = 3.5$.

For the scattering amplitude, we may simply evaluate $W_{\eta_s, 2D}(k_r)$ at the Bragg wavenumber, $k_r = 2k_0$. However, for the long-wavelength interface roughness, we need the 1-D spectrum along the x-axis, $W_{\eta_s, 1D}(K)$. We do this by taking the 1-D transform of $W_{\eta_s, 2D}(K, L)$ along the slice $y = 0$,

$$W_{\eta_s, 1D}(K) = \int_{-\infty}^{\infty} W_{\eta_s, 2D}(K, L) dL. \quad (3.5a)$$

In cylindrical coordinates, we have

$$\begin{aligned}
 W_{\eta_s, 1D}(K) &= 2 \int_K^{\infty} \frac{k_r}{\sqrt{k_r^2 - K^2}} W_2(k_r) dk_r \\
 &= \gamma \sigma^2 L_{corr} (1 + L_{corr}^2 K^2)^{\frac{\beta_\eta + 1}{2}},
 \end{aligned} \tag{3.5b}$$

where

$$\gamma = \frac{\left(\frac{\beta_\eta}{2} - 1\right) \Gamma\left(\frac{1}{2}\right) \Gamma\left(\frac{\beta_\eta}{2} - \frac{1}{2}\right)}{\pi \Gamma\left(\frac{\beta_\eta}{2}\right)}. \tag{3.5c}$$

We now have to transform a random realization of the corresponding 1-D amplitude spectrum which has been scaled by a random amplitude and phase. In other words, we define the realization as

$$\eta(x) = \int_{-\infty}^{\infty} S_{\eta_s, 1D}(K) e^{iKx} dK \tag{3.6a}$$

where

$$S_1(K) = [W_{\eta_s, 1D}(K)]^{1/2} A(K) e^{i\theta(K)}, \tag{3.6b}$$

and A and θ are random numbers for all values of K . Since the complex amplitude of each wavenumber component, $Ae^{i\theta}$, should exhibit a normal distribution, the random phase of each component can be obtained from

$$\theta = 2\pi r_1, \tag{3.7a}$$

where r_1 is a uniformly distributed random variable in the interval $[0,1]$. The magnitude A , however, exhibits a Rayleigh distribution. Because we are in fact generating a realization of the power spectrum, we must consider the magnitude-squared, which has a negative exponential distribution. The random amplitude of each wavenumber component is then obtained by

$$A = \sqrt{-\ln(r_2)}, \quad (3.7b)$$

where r_2 is another independent, uniformly distributed random variable in the interval $[0,1]$.

In practice, we could simply use

$$W_{\eta_s, 1D}(K) = (1 + L_{corr}^2 K^2)^{-\frac{\beta_\eta}{2} + \frac{1}{2}} \quad (3.8a)$$

and rescale the result by its rms value, i.e. $\frac{\eta(x)}{\langle \eta^2(x) \rangle^{1/2}}$, or we could simply say

$$W_{\eta_s, 1D}(K) \propto (1 + L_{corr}^2 K^2)^{-\frac{\beta_\eta}{2} + \frac{1}{2}} \quad (3.8b)$$

where L_{corr} and β_η had to be specified. This was the generic spectral model used in generating the realizations first in MATLAB and then for implementation in the MMPE model.

2. Volume Sound Speed Fluctuations

Unlike spatial variations of the interface, volumetric variations are generally 3-D in nature. We will now treat the generation of volumetric variations through spectral realizations as in the interface. The sediment volume sound speed perturbations may be modeled by a 3-D volume spectra (Yamamoto, 1995) given by

$$W_{\delta_s, 3D}(K, L, M) = \frac{\beta_\delta \Lambda^2 B}{2\pi} \left(\Lambda^2 (K^2 + L^2) + M^2 \right)^{-\frac{\beta_\delta}{2} - 1} \quad (3.9)$$

where B is the spectral strength constant, β_δ is the spectral exponent, and $\Lambda = \frac{a_3}{a_1} = \frac{a_3}{a_2}$ is

the horizontal-to-vertical aspect ratio describing the anisotropy of fluctuations in the sediment. We shall assume the major axis corresponding to M is aligned with the vertical, thus we neglect any “dip” angle in the structure. M is thus the vertical wavenumber.

From Yamamoto's findings, we shall assume the following values:

$$\begin{aligned}\beta_\delta &\sim 2, \\ B &\sim 5 \times 10^{-4}, \\ \Lambda &\sim 5.\end{aligned}\tag{3.10}$$

This should produce a relative velocity variance of $\sim 10^{-4}$. Also note in this form that we really assume $K = h_0 k_x$ where $h_0 = 1\text{m}$ is simply a reference length so that K, L, M are unitless and units of $W_{\delta_s, 3D}$ do not depend on β .

Recalling Eq. (2.66b), in order to evaluate the scattering due to the volume perturbations, we need a representation for the volume spectra in the 2-D horizontal plane. Hence for our reverberation computations, we have

$$W_{\delta_s, 2D_H}(K, L) = \int_{-\infty}^{\infty} W_{\delta_s, 3D}(K, L, M) dM.\tag{3.11}$$

Note that we are effectively evaluating the 3-D spectra at a single depth, since it is delta-function correlated. Substituting Eq. (3.9) into (3.11), we obtain,

$$\begin{aligned}W_{\delta_s, 2D_H}(K, L) &= \int_{-\infty}^{\infty} W_{\delta_s, 3D}(K, L, M) dM \\ &= \frac{\beta_\delta \Lambda^2 B}{\pi} \int_0^{\infty} [\Lambda^2 (K^2 + L^2) + M^2]^{\frac{\beta_\delta - 1}{2}} dM \\ &= \frac{\beta_\delta \Lambda^2 B \sqrt{\pi}}{2\pi} [\Lambda^2 (K^2 + L^2)]^{\frac{\beta_\delta - 1}{2}} \frac{\Gamma\left(\frac{\beta_\delta}{2} + \frac{1}{2}\right)}{\Gamma\left(\frac{\beta_\delta}{2} + 1\right)}.\end{aligned}\tag{3.12}$$

For $\beta_\delta = 2$, Eq. (3.12) can also be shown to reduce simply to

$$\begin{aligned}W_{\delta_s, 2D_H}(K, L) &= \frac{2\Lambda^2 B}{\pi} \int_0^{\infty} [\Lambda^2 (K^2 + L^2) + M^2]^{-2} dM \\ &= \frac{\Lambda^2 B}{2} [\Lambda^2 (K^2 + L^2)]^{-\frac{3}{2}}.\end{aligned}\tag{3.13}$$

For the values of B and Γ in Eq. (3.10) chosen, this reduces to

$$W_{\delta_s, 2D_H}(K, L) = \alpha (K^2 + L^2)^{-\frac{3}{2}} \quad (3.14a)$$

where

$$\alpha = \frac{B}{2\Lambda} = 5 \times 10^{-5}. \quad (3.14b)$$

Note that the above provides the 2-D *horizontal* spectrum which is needed to evaluate the reverberation. However, to compute the forward propagation, we need the 2-D *vertical* spectrum in the (r, z) plane. In other words, we will now perform the integration cross-range at $y = 0$, giving

$$\begin{aligned} W_{\delta_s, 2D_V}(K, M) &= \int_{-\infty}^{\infty} W_{\delta_s, 3D}(K, L, M) dL \\ &= \frac{\beta_s \Lambda^2 B}{2\pi} \int_{-\infty}^{\infty} [\Lambda^2 (K^2 + L^2) + M^2]^{-\frac{(\beta_s+2)}{2}} dL. \end{aligned} \quad (3.15)$$

For $\beta_s = 2$, this in turn reduces to

$$\begin{aligned} W_{\delta_s, 2D_V}(K, M) &= \frac{\Lambda B}{2} [\Lambda^2 K^2 + M^2]^{-\frac{3}{2}} \\ &= \alpha' [25K^2 + M^2]^{-\frac{3}{2}} \end{aligned} \quad (3.16a)$$

where

$$\alpha' = 1.25 \times 10^{-3}. \quad (3.16b)$$

To generate 2-D vertical volume fluctuation realizations, we do essentially the same thing as in the case of the interface. Since we are looking at sound speed perturbations, we define a realization as

$$c_0 \delta(x, z) = \iint S_{\delta_s, 2D_V}(K, M) e^{iKx} e^{iMz} dK dM \quad (3.17a)$$

where

$$S_{\delta_s, 2D_v}(K, M) = [W_{\delta_s, 2D_v}(K, M)]^{1/2} A(K, M) e^{i\theta(K, M)}. \quad (3.17b)$$

Notice that since we have treated sound speed perturbations in the volume in the *vertical*, we really are generating a series of *vertical* realizations at each range step.

In similar fashion to the interface, we define the 2-D random phase variations as

$$\theta(K, M) = 2\pi r_1(K, M), \quad (3.18a)$$

where $r_1(K, M)$ is now a *matrix* of uniformly distributed random numbers in $[0, 1]$, and the amplitude variations are

$$A(K, M) = \sqrt{-\ln(r_2(K, M))}, \quad (3.18b)$$

where $r_2(K, M)$ is another matrix of uniformly distributed random numbers in $[0, 1]$. In practice, we use

$$W_{\delta_s, 2D_v}(K, M) \propto (\Lambda^2 K^2 + M^2)^{\frac{\beta_\delta - 1}{2}}, \quad (3.19)$$

where Λ and β_δ are to be specified in generating the realization. The final result for the volume perturbation is then rescaled by the desired rms value.

3. Spectral Filter

We must note that both the interface and volume realizations will need to be filtered at low and high wavenumbers in order to reduce edge effects, which will introduce additional unwanted spectral components. The filter is also used to extract the pertinent portions of both the interface and volume spectra for creation of the long-wavelength realization affecting the forward propagation.

At the low end, we can assume scales greater than 500m are known. As such,

$$k_{\min} \approx \frac{2\pi}{500} \approx 0.1. \quad (3.20a)$$

At the high end, we should compute up to about the acoustic wavelength, so

$$k_{\max} \approx k_0 = \frac{2\pi f}{c_0}, \quad (3.20b)$$

which will depend on our frequency of calculation. In a broadband computation, c_0 will be our center frequency.

B. IMPLEMENTATION OF THE INTERFACE AND VOLUME SPECTRAL DESCRIPTIONS IN MMPE

As the MMPE is well documented (Smith, 2000), a quick run-through will be afforded in order to understand the integration of the spectral perturbation model into the MMPE. However, before any implementation was possible, MATLAB was used to test the model and its algorithm.

1. Description of MMPE

The $N \times 2D$ MMPE model (Smith, 2000) is based on the split-step Fourier algorithm developed in the UMPE model (Smith and Tappert, 1994) written in FORTRAN '95. MMPE generates the environmental propagator, U_{op} , in a subroutine called "ENVPROP" using the bottom bathymetric and sound speed data. These data points are interpolated to fit the depth points being computed at each range step. ENVPROP is subsequently called at each range to generate the propagator variations due to a range-dependent environment specified in the input files. In the case where there are perturbations, the program is 'forced' to think that it is in a range-dependent environment.

Several input files are used to specify pertinent input parameters, most important of all being the file named "pefiles.inp." In there, several input filenames are specified, one each for the source parameters, sound speed profile(s), bathymetric data set(s), bottom properties (like shear and compressional sound speeds, etc.), a sub-layer bathymetry, and the sub-layer properties. A total of seven input files are used for running MMPE simulations.

2. FORTRAN & MATLAB Implementation of Perturbation Models

Before actual implementation of Eqs. (3.8b) and (3.19) into the MMPE's FORTRAN code, MATLAB was used to code up and test the algorithm and effects of generating different roughness and perturbation rms values. These were proven successful, with the expected spatial and sound speed perturbations modeled effectively. A "tweaking" factor for each type of perturbation was used, namely the rms roughness and the rms sound speed variations, to allow observation of these perturbations.

Subsequently, these algorithms were translated and implemented into the MMPE, now renamed "MMPEREV." In MMPEREV, two additional subroutines are called within the subroutine "ENVPROP1" to introduce perturbations. "ZBGEN" introduces the spatial perturbation to the bottom bathymetry at each range step while "DCGEN" introduces the sound speed perturbation to the volume at each depth grid point and range step. ENVPROP1 is then made to think that a range-dependent case is present simply because the perturbations cause irregularities in depth and sound speed, causing the program to call ENVPROP at each range step.

A random number generator was used in FORTRAN to provide the uniformly distributed random numbers in the range [0,1]. Each time the random number is required, a series is generated. However, each time the compiled MMPEREV program is started, the same seed is used by FORTRAN so that the same set of random numbers are invoked. Thus, the same sequence of random numbers is used for each run, allowing for controlled analysis of the results. This is described later. Later implementations to MMPEREV will allow for the generation of a random seed in order to effectively model truly random fluctuations to the intended data set. Some results of the controlled analysis are seen in the next sub-section.

3. Results of Varying RMS Values to Perturbations

We now present some results from the random fluctuations to bottom bathymetry in range by varying the root-mean-square values of the interface spatial perturbations.

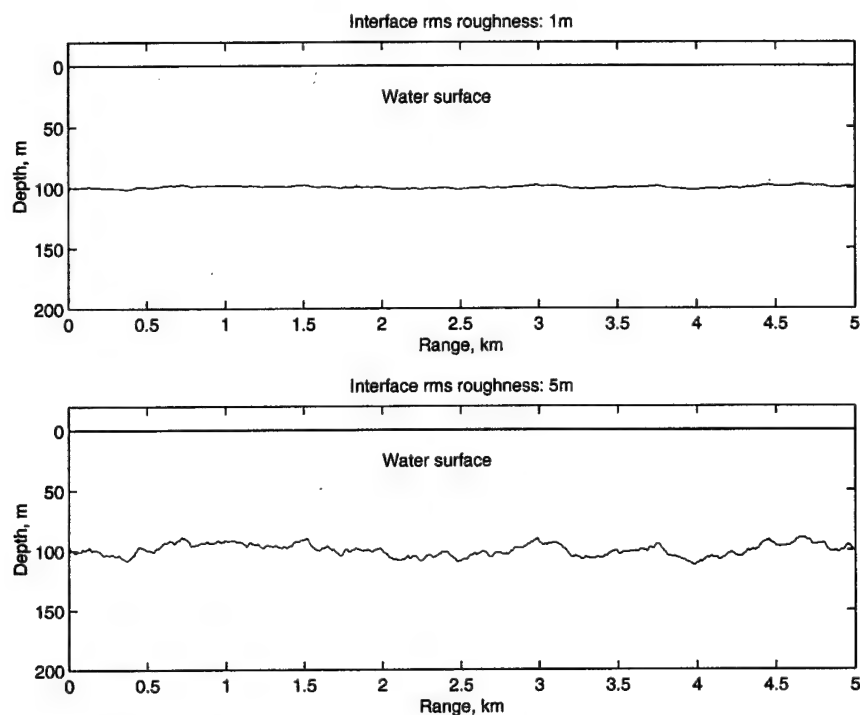


Figure 3.1 – Plot of Interface Roughness of Different rms Values

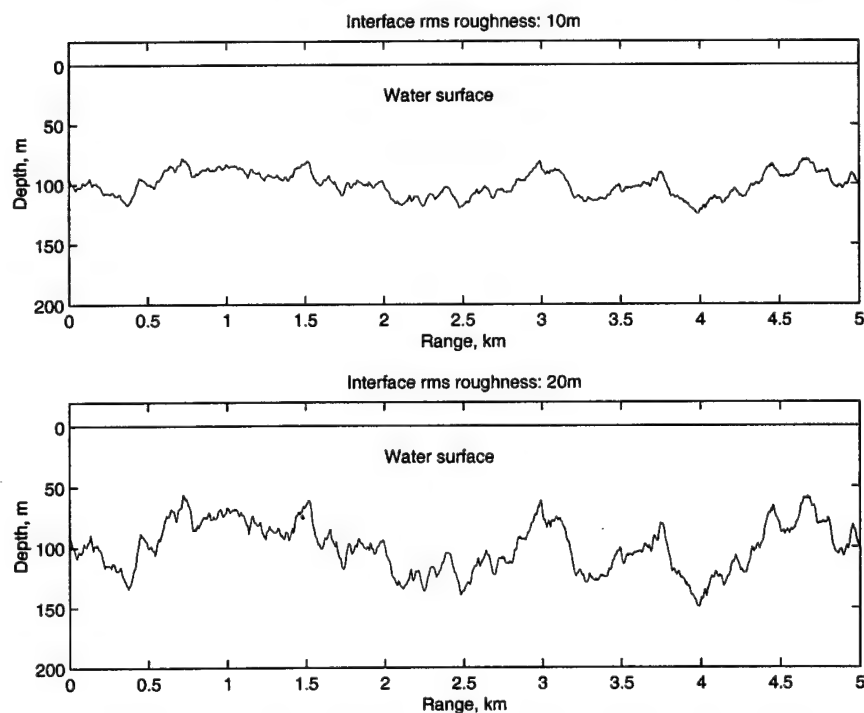


Figure 3.2 – Plot of Interface Roughness of Higher rms Values

From Figure 3.1 and Figure 3.2, increased rms roughness is seen as the root-mean-square values are increased. The longer wavelength perturbations also become more distinct. A cursory survey of shallow water areas, especially in the East China Sea where the ASIAEX experiment will be conducted, reveals that the long wavelength components are relatively small. Hence, an rms value of 1m was selected.

Effects of tweaking volumetric root-mean-squared perturbations to the sound speed follows. The mean bottom sediment sound speed selected was 1700 m/s, which is normal for a sand/mud layer.

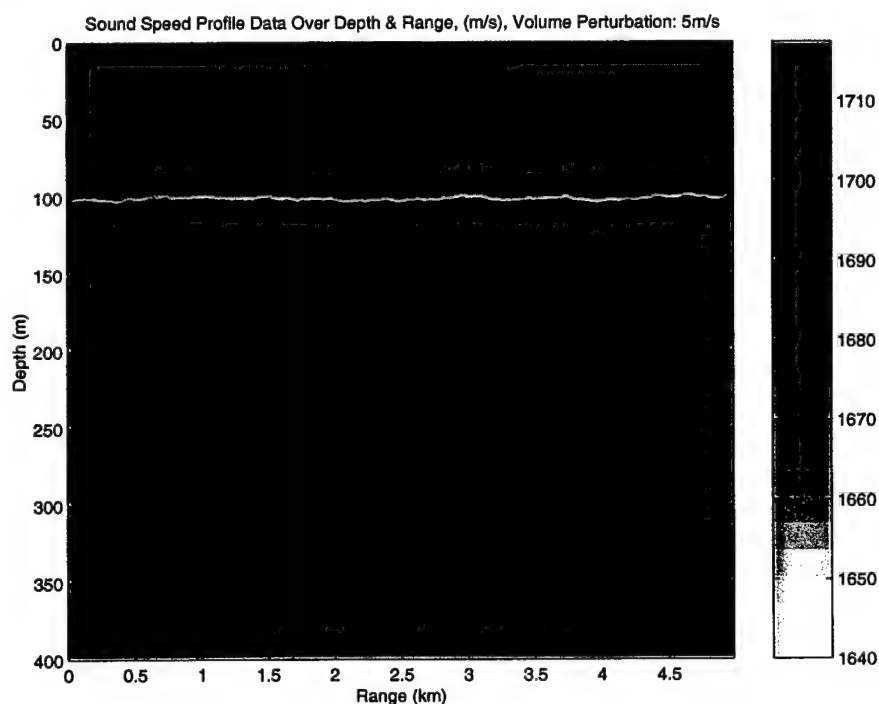


Figure 3.3 – SSP Data with Volume Sound Speed Perturbation of 5 m/s and Interface Perturbation of 1 m

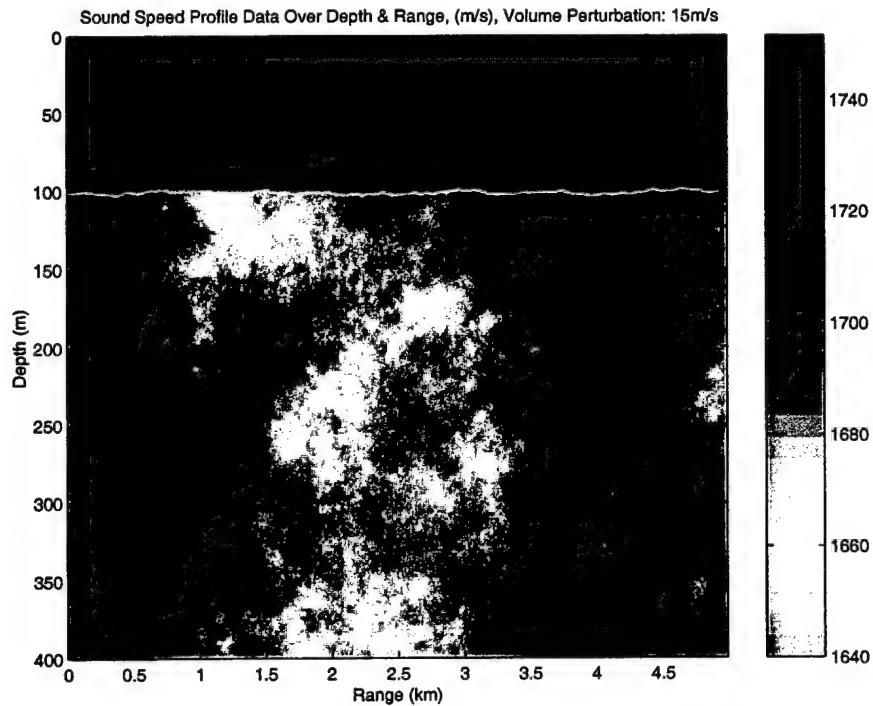


Figure 3.4 – SSP Data with Volume Sound Speed Perturbation of 15 m/s and Interface Perturbation of 1 m

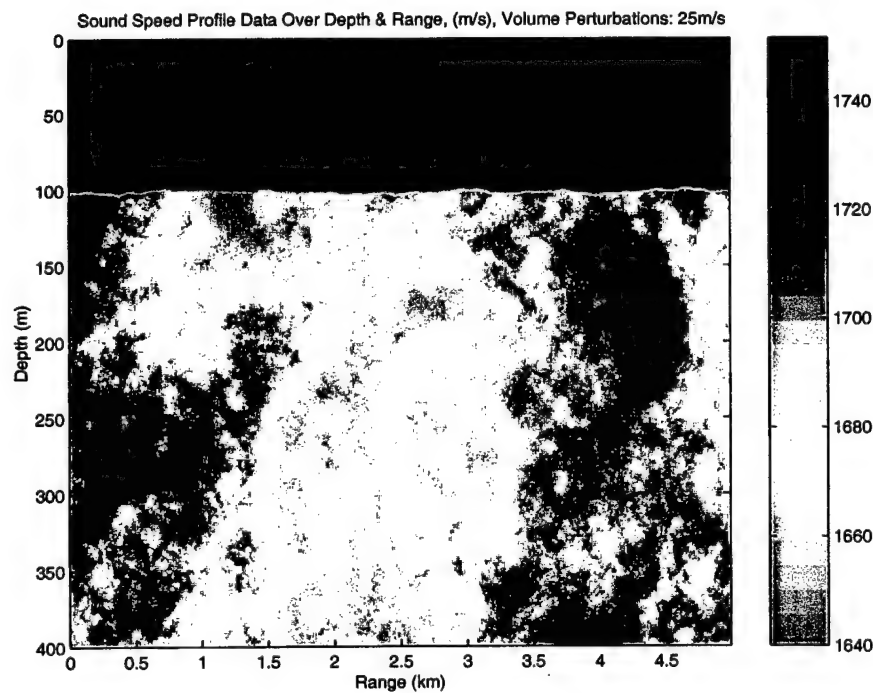


Figure 3.5 – SSP Data with Volume Sound Speed Perturbation of 25 m/s and Interface Perturbation of 1 m

Apparent from Figure 3.3 through Figure 3.5 is the increasing contrast in the sound speed profile for an increasing sound speed rms perturbation when comparing them qualitatively. While it is not likely that the sediment layer is homogeneous, as in Figure 3.3 (rms perturbation being 5 m/s), it is not unimaginable that the sound speed profile can vary considerably due to inhomogeneities and mixture of different sediment types. A median sound speed perturbation of 15 m/s (Figure 3.4) was finally used for the follow-on analysis. Notice also that the interface rms roughness used was 1 m.

THIS PAGE IS INTENTIONALLY LEFT BLANK

IV. POST-PROCESSING IMPLEMENTATIONS IN MATLAB AND SIMULATION RESULTS

The second and final step in our modeling efforts was the development of post-processing routines to extract the relevant data from two, one-way propagation data sets generated by MMPEREV (see Chapters II and III) and then compute reverberation and perform signal analyses on the derived data. We will also see that the time-domain convolution of the two one-way field functions will give the time-domain reverberation structure received for both monostatic and bistatic setups. Routines were written to perform signal processing on these reverberation data sets. Specifically, this chapter will expand on the work done to derive the following:

- reverberation loss for broadband signals (time-series) and CW signals (range-series);
- vertical correlation and peak correlation computation; and
- spectral analyses.

We saw from Chapter II, Sections B and C that a scaling or normalization due to the wave scattering strength is needed in order to arrive at the reverberation loss. However, we will not attempt to introduce any scaling here, as these normalization factors are assumed to be constants (see Eqs (2.50) and (2.66b) for CW analyses, and Eqs. (2.68b), (2.68c) and (2.71) for time-domain analyses).

Discussion of the reverberation computation cannot be made without first defining the geometrical and environmental setup of the modeling effort. Of interest was the particular configuration and environmental parameters likely to be used in ASIAEX.

A. MODELING ENVIRONMENT AND GEOMETRY

Since the varying spatial properties of the broadband signal are of interest, an array was typically chosen in collecting field data. Each element of the vertical line array (VLA) was assumed to be a point source and the array was located vertically in the water column. The MMPE/MMPEREV model provided as an output the field function for the entire water column and bottom volume up to a given range. The fluctuations in the bottom bathymetry and volume sound speed were randomly generated by MMPEREV as explained in Chapter III.

1. Multi-static Reverberation Geometry

In the analyses, there was a requirement to develop a geometry able to support both monostatic and bistatic reverberation computations/measurements. As such, a 16-element VLA was used in the modeling effort. Figure 4.1 shows the VLA and its geometry relative to a given scattering patch at horizontal range r . We see that the mean horizontal distance of the VLA to a small scattering patch is r , in see Eq. (2.43).

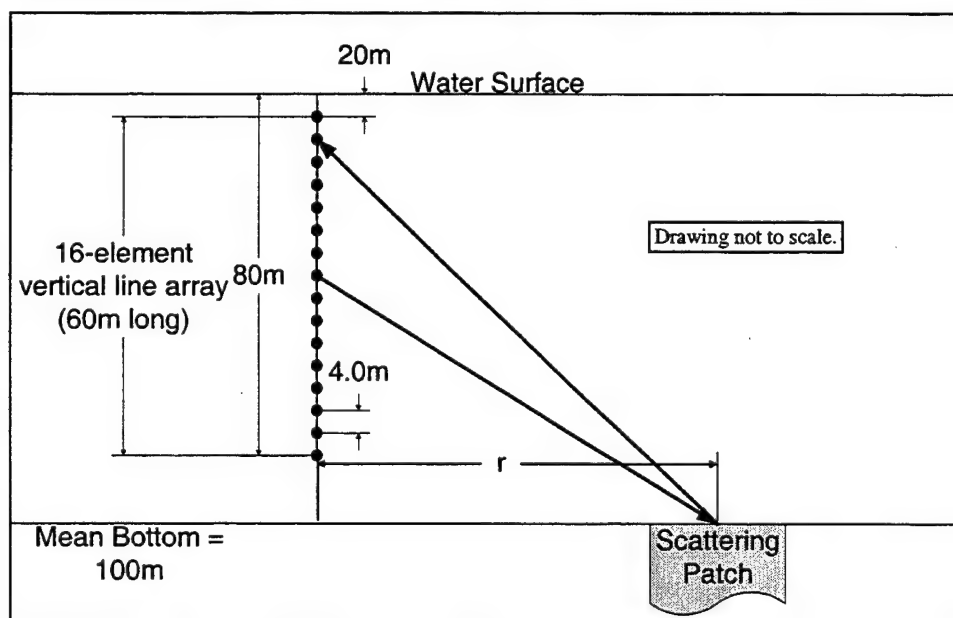


Figure 4.1 – Geometry of VLA and Scattering Patch

From Figure 4.1, we see that the 16-element VLA spans the water column from 20 m to 80 m with the array elements located 4 m apart in depth. A single element at 48 m depth (or element number 8 from the top) was chosen as the source with all 16 elements receiving the reverberation.

As there was a need to isolate source/receiver pairs, MMPEREV was set to generate 16 sets of output files using each array element as a reciprocal source and then propagating the field through the entire space with the environmental and source parameters specified in the next sub-section.

2. The Environment

The maximum propagation range was selected to be 5 km. In a shallow water environment, the mean bottom depth was assumed to be 100 m with no mean slope. To perform broadband as well as CW analysis, a center frequency of 250 Hz was chosen with a 250 Hz bandwidth divided into 512 discrete propagation frequencies. The frequency span was from 124.7554 through 374.7554 Hz computed automatically by MMPEREV. Seven control and environmental input files were required by MMPE/MMPEREV to perform the computations. In order to properly define the environment for running the MMPEREV model, there was a need to define the baseline features of frequency, depth, grid (depth and range), etc.

In order that the time steps and range steps coincide appropriately for coherent addition as needed, we start by seeing that in reduced time at the m^{th} range step, we have

$$T_m = t_m - \frac{r_m}{c_0}, \quad (4.1)$$

where T_m is reduced time, t_m is true time at range step m , r_m is the range, and c_0 is the reference sound speed. Hence,

$$t_m = T + \frac{r_m}{c_0}. \quad (4.2)$$

Now, true time at r_{m+1} is

$$t_{m+1} = T + \frac{r_{m+1}}{c_0} = T + \frac{r_m + \Delta r}{c_0} , \quad (4.3)$$

where Δr is the range step size (not the MMPEREV computation range step size, which will be notated as δr), which leads to

$$t_{m+1} - t_m = \frac{\Delta r}{c_0} . \quad (4.4)$$

The frequency step is defined by

$$\Delta f = \frac{BW}{nf - 1} , \quad (4.5)$$

where nf is the number of frequencies we would like to compute in a broadband scenario with BW being the bandwidth selected. The time increment then becomes

$$\Delta t = \frac{T}{nf - 1} = \frac{1}{(nf - 1)\Delta f} = \frac{1}{BW} . \quad (4.6)$$

Suppose we want a bandwidth of 250 Hz, a center frequency of 250 Hz, and a frequency step size of about 1/2 Hz, then selecting

$$\Delta t = \frac{1}{250} = 4 \text{ ms} , \quad (4.7)$$

we get

$$\begin{aligned} nf &= 512 , \\ \Delta f &= \frac{250}{511} = 0.49 \text{ Hz} . \end{aligned} \quad (4.8)$$

Note that nf has to be a radix-2 integer because of the Fast-Fourier Transform (FFT) that was used to compute spectral components in MMPEREV and in the MATLAB post-processing.

We now constrain the range step to be an integer multiple of the MMPEREV computational range step size by defining

$$\Delta r = k \times \delta r, \quad (4.9)$$

where k is an arbitrary integer to constrain the relationship with the MMPEREV computation range step size, δr . By forcing this constraint, we have defined the spatial resolution of the generated solution to explicitly overlap the temporal resolution. This will allow us to easily combine solutions from different range steps coherently in the time-domain.

To resolve time, we also define

$$\frac{\Delta r}{c_0} = j \times \Delta t, \quad (4.10)$$

where j is another arbitrary integer to constrain the time-range relationship for the purpose of computations in MMPEREV. For $\Delta t = 4 \text{ ms}$, selecting $j = k = 1$ and $c_0 = 1500 \text{ m/s}$, we get

$$\begin{aligned} \Delta r &= 6 \text{ m}, \\ \delta r &= 6 \text{ m}. \end{aligned} \quad (4.11)$$

Hence for a given maximum range of 5 km, the number of range steps to be computed is

$$nr = \frac{5000}{6} \approx 833 \quad (4.12)$$

in MMPEREV. Note that the maximum computational range will then be $r_{\max} = 4.998 \text{ km}$.

Finally, we select the number of total computational depth points to be 256, which would also determine the FFT-size for the split-step Fourier algorithm, also a radix-2 integer. This provides a vertical spatial resolution for computation of roughly 3 m. The following table summarizes the environmental parameters used in the modeling in MMPE, noting that much of the parameters used for the bottom and deep-bottom properties were assumed.

Filename/Parameter	Value	Remarks
Main Control File: pefiles.inp		
Number of depth points	256	Radix-2 integer required
Minimum depth	0 m	
Maximum depth	400 m	
Number of range steps	833	
Minimum range	0 m	
Maximum range	5.0 km	
Range step size	6 m	
Maximum computed depth	400 m	
Reference sound speed	1500 m/s	
Source File: pesrc.inp		
Source depths	Varying	Array elements at 20, 24, 28, 32, 36, 40, 44, 48, 52, 56, 60, 64, 68, 72, 76 and 80 m depths.
Center frequency	250 Hz	
Frequency bandwidth	250 Hz	
No. of Frequencies	512	Radix-2 integer required
Sound Speed File: pessp.inp		
Water column sound speed	1500 m/s	Range independent
No. of SSPs	1	
Bathymetry: pebath.inp		
Mean bottom depth	100 m	Range independent
No. of depth points	1	
Bottom properties: pebotprop.inp		
Bottom sound speed	1700 m/s	
Sound speed gradient	0	
Relative density	1.0	No density variations
Compressional attenuation	0.2 dB/km/Hz	
Shear speed	0	Not modeled
Shear attenuation	0	Not modeled
Deep Bottom Bathymetry: pedbath.inp		
Depth	3000 m	
Deep Bottom Properties: pedbotprop.inp		
Deep bottom sound speed	2000 m/s	
Sound speed gradient	0	
Relative density	3.0	No density variations
Compressional attenuation	0.25 dB/km/Hz	
Shear speed	0	Not modeled
Shear attenuation	0	Not modeled
RMS Perturbations (input to MMPEREV during run)		
Interface	1 m	As explained in Chapter III
Volume	15 m/s	

Table 4.1 – MMPEREV Input Environmental Properties

3. MMPE and MMPEREV Runs

With the propagation environment specified, MMPEREV was setup to make 16 runs, each for a different source depth from 20-80 m at 4 m increments in depth. The ability to propagate the same signal out from the various receivers to the scattering patch is based on reciprocity as explained in Chapter II, and using Eq. (2.68b) we are able to arrive at the reverberant field. As such, 16 output binary files for the configuration above were computed and stored. In order to make comparisons with the unperturbed data, MMPE was also setup to make 16 runs for the same array element depths based on the same environmental conditions shown in Table 4.1. The following table summarizes the filenames used.

Receiver /Source Depth	MMPEREV Output File (perturbed data)	MMPE Output File (unperturbed data)
20m	peoutzbrmsldcrms15s20.bin	peouts20.bin
24m	peoutzbrmsldcrms15s24.bin	peouts24.bin
28m	peoutzbrmsldcrms15s28.bin	peouts28.bin
32m	peoutzbrmsldcrms15s32.bin	peouts32.bin
36m	peoutzbrmsldcrms15s36.bin	peouts36.bin
40m	peoutzbrmsldcrms15s40.bin	peouts40.bin
44m	peoutzbrmsldcrms15s44.bin	peouts44.bin
48m	peoutzbrmsldcrms15s48.bin	peouts48.bin
52m	peoutzbrmsldcrms15s52.bin	peouts52.bin
56m	peoutzbrmsldcrms15s56.bin	peouts56.bin
60m	peoutzbrmsldcrms15s60.bin	peouts60.bin
64m	peoutzbrmsldcrms15s64.bin	peouts64.bin
68m	peoutzbrmsldcrms15s68.bin	peouts68.bin
72m	peoutzbrmsldcrms15s72.bin	peouts72.bin
76m	peoutzbrmsldcrms15s76.bin	peouts76.bin
80m	peoutzbrmsldcrms15s80.bin	peouts80.bin

Table 4.2 –MMPEREV/MMPE Output Files

We can, from a single CW run of MMPE and MMPEREV, make qualitative comparisons of the effects of the interface and volume perturbations.

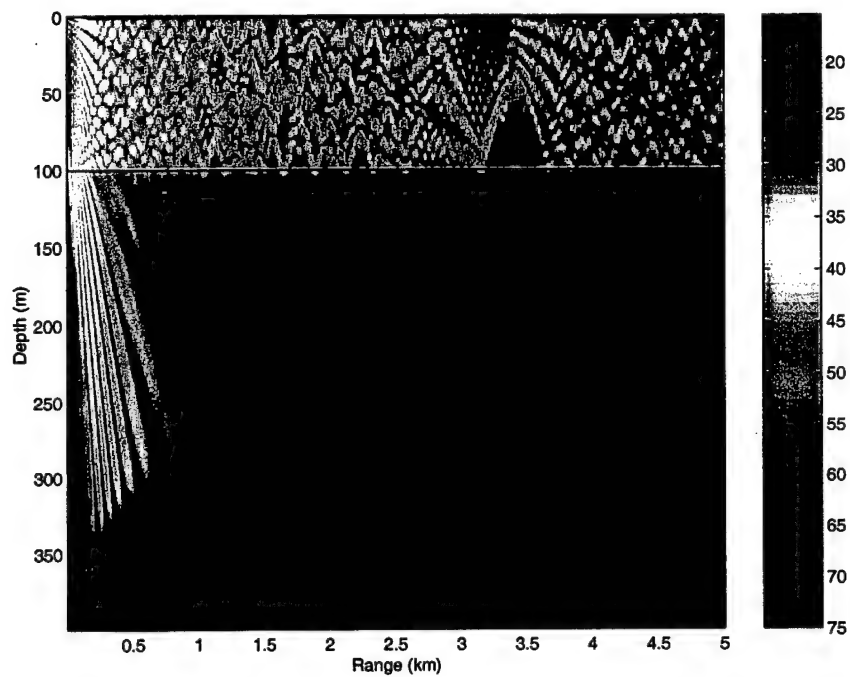


Figure 4.2 – Transmission Loss (dB re 1 m) with No Perturbation,
Source: 48 m, Frequency: 250 Hz

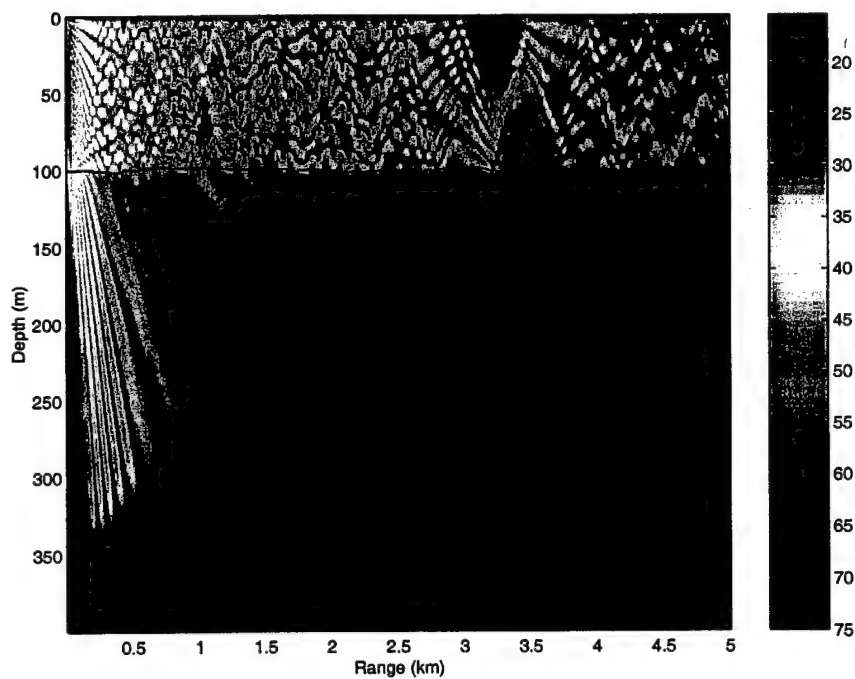


Figure 4.3 – Transmission Loss (dB re 1 m) with Perturbation,
Source: 48 m, Frequency: 250 Hz

When the perturbation was introduced, the structure in Figure 4.2 was disrupted as shown in Figure 4.3. The dispersed penetration into the volume is also apparent. In the next few sections, we will discuss the post-processing implemented to compute reverberation, vertical correlation, and spectral analysis.

B. POST-PROCESSING 1 – REVERBERATION (MATLAB IMPLEMENTATION)

Recall that in Chapter II we derived the CW reverberant field for a scattering patch due to the interface and volume in Eqs. (2.33) and (2.61), respectively. In order to arrive at the reverberant field at the receiver due to a co-located or displaced source, we had to find the interactions of these fields over the entire scattering area. We will also perform broadband and CW computations by utilizing the same output from MMPEREV set to run on the various geometrical configurations for the VLA described in the previous sub-section. Again, we were able to separate the bottom interface and bottom volume analyses because of their different perturbations. The separate analysis also afforded closer discrimination of the structure of one independently of the other.

The source was located at 48 m depth, which was in the vicinity of the center of the water column. Each of the array elements (including the 48 m array element) were then treated as independent receivers. Each of the output files from MMPEREV and MMPE could be paired with the output file for the 48 m source depth binary files for computation. Naturally, the 48 m source and 48 m receiver files were the same binary file, meaning a monostatic geometry while the other transmitter/receiver pairs reflected a vertical bistatic geometry.

Both perturbed and unperturbed data generated using MMPEREV and MMPE, respectively, were analyzed to provide useful comparisons and further analyses. We will also show the results for each analysis performed.

1. Two-way Mono/Bistatic CW Reverberation Analysis

For the interface, we have from Eq. (2.33) and subsequently in Eq. (2.43),

$$\langle |p_-|^2 \rangle \approx \frac{B}{r^2} |\psi_{Tb}(r)|^2 |\psi_{Rb}(r)|^2 k_r^2 W_{\eta_s, 2D}(k) \Delta A_b. \quad (4.13)$$

This is simply proportional to the magnitude-squared of the forward and backward propagated field functions. As the perturbation spectrum and other field constants are generated by MMPEREV, the MATLAB post-processing that computes the CW reverberation is just the multiplication of the magnitude-squared field functions with cylindrical spreading,

$$|p_-| \propto \left| \frac{\psi_{Tb}(r)}{\sqrt{r}} \right| \left| \frac{\psi_{Rb}(r)}{\sqrt{r}} \right|, \quad (4.14)$$

and the interface reverberation loss (RL_b) is then

$$RL_b(r) = A - 20 \log \left[\frac{|\psi_{Tb}(r)| |\psi_{Rb}(r)|}{r} \right], \quad (4.15)$$

where A is a constant which accounts for the other parameters in Eq. (2.50).

The volume was also treated as described in Eq. (2.66b) and the volume reverberation loss may be written as

$$RL_v(r) = B - 20 \log \left[\frac{1}{r} \int_{z=z_b}^{\infty} \hat{n}(r, z) |\psi_T(r, z)| |\psi_R(r, z)| dz \right], \quad (4.16)$$

where B is another constant which accounts for the other terms in Eq. (2.66b). Using now the same 16 sets of results from a single MMPEREV and another 16 sets of results from the MMPE runs, we post-processed the field function information to arrive at the CW interface and volume analyses. We have selected the minimum, center and maximum frequencies for analysis. The MATLAB files written to post-process the MMPEREV/MMPE output files to arrive at the CW analysis are given in Table 4.3. The output from each run of `peout2way_bistat_r.m` was saved as a MATLAB data file so that the data set could be loaded into the MATLAB workspace without having to re-process the MMPEREV/MMPE output binary files. The filenames saved are listed in Table 4.5.

MATLAB Post-Processing Files Description	Perturbed Data Processing Files	Unperturbed Data Processing Files
Binary file data extractor: Opens both source and receiver binary files (output from MMPE/MMPEREV) and all modeling data. Stores them on the MATLAB workspace.	peout1_bistat_r.m	peout1_bistat_np_r.m
Interface and Volume Reverberation loss Computation: Extracts field data source and receiver files at selected frequencies. Computes the two-way reverberation loss for the interface and volume as described above. Extracts field data at f_{min} , f_{center} and f_{max} .	peout2way_bistat_r.m	peout2way_bistat_np_r.m

Table 4.4 – MATLAB Filenames Created for CW Reverberation Analysis

Receiver Depth	Interface Perturbed Data Ouput	Volume Perturbed Data Ouput	Interface Unperturbed Data Ouput	Volume Unperturbed Data Ouput
20m	bistat4820int_r.mat	bistat4820vol_r.mat	bistat4820int_np_r.mat	bistat4820vol_np_r.mat
24m	bistat4824int_r.mat	bistat4824vol_r.mat	bistat4824int_np_r.mat	bistat4824vol_np_r.mat
28m	bistat4828int_r.mat	bistat4828vol_r.mat	bistat4828int_np_r.mat	bistat4828vol_np_r.mat
32m	bistat4832int_r.mat	bistat4832vol_r.mat	bistat4832int_np_r.mat	bistat4832vol_np_r.mat
36m	bistat4836int_r.mat	bistat4836vol_r.mat	bistat4836int_np_r.mat	bistat4836vol_np_r.mat
40m	bistat4840int_r.mat	bistat4840vol_r.mat	bistat4840int_np_r.mat	bistat4840vol_np_r.mat
44m	bistat4844int_r.mat	bistat4844vol_r.mat	bistat4844int_np_r.mat	bistat4844vol_np_r.mat
48m	bistat4848int_r.mat	bistat4848vol_r.mat	bistat4848int_np_r.mat	bistat4848vol_np_r.mat
52m	bistat4852int_r.mat	bistat4852vol_r.mat	bistat4852int_np_r.mat	bistat4852vol_np_r.mat
56m	bistat4856int_r.mat	bistat4856vol_r.mat	bistat4856int_np_r.mat	bistat4856vol_np_r.mat
60m	bistat4860int_r.mat	bistat4860vol_r.mat	bistat4860int_np_r.mat	bistat4860vol_np_r.mat
64m	bistat4864int_r.mat	bistat4864vol_r.mat	bistat4864int_np_r.mat	bistat4864vol_np_r.mat
68m	bistat4868int_r.mat	bistat4868vol_r.mat	bistat4868int_np_r.mat	bistat4868vol_np_r.mat
72m	bistat4872int_r.mat	bistat4872vol_r.mat	bistat4872int_np_r.mat	bistat4872vol_np_r.mat
76m	bistat4876int_r.mat	bistat4876vol_r.mat	bistat4876int_np_r.mat	bistat4876vol_np_r.mat
80m	bistat4880int_r.mat	bistat4880vol_r.mat	bistat4880int_np_r.mat	bistat4880vol_np_r.mat

Table 4.5 – Processed Output Data Files in CW Analysis

2. CW Analysis Results

A typical CW reverberation loss plot shows a $20 \log r$ (two-way cylindrical spreading) drop in range. Figures 4.4 and 4.5 show the interface and volume reverberation loss for a source depth of 48 m, receiver depth of 40 m and frequency of 250 Hz. In all cases, the constant scaling parameters A and B were set equal to zero. With the same source and receiver depths and at the same center frequency, we were able to observe finer structures in the interface reverberation (Figure 4.4) compared to the volume reverberation plot (Figure 4.5). This was because multiple incoherent

multiplications were performed at all depths and then summed vertically in order to arrive at the mean squared RPL at the receiver due to the volume. Note that all data sets show very little energy interacting with the interface or volume at very short ranges, i.e. $\leq 0.1\text{km}$. This is due to the wide-angle limitation of the parabolic approximation.

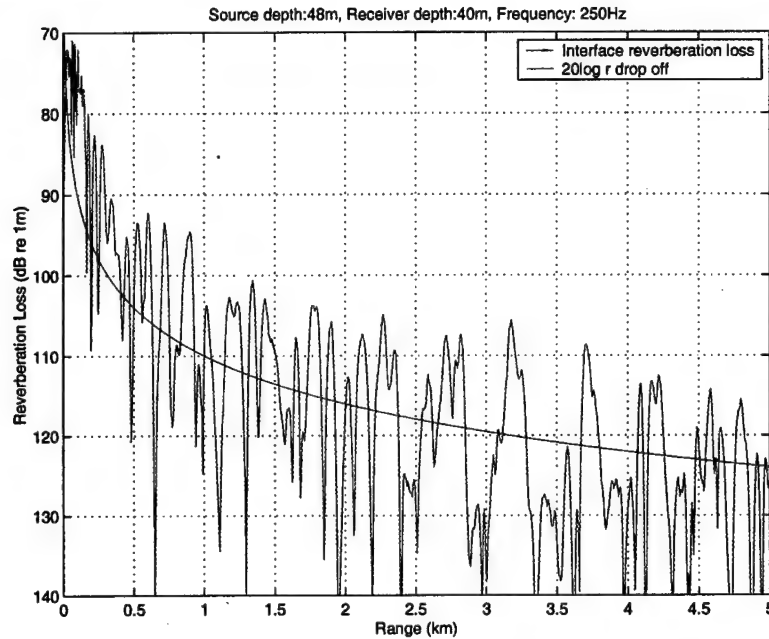


Figure 4.4— Interface Reverberation Loss for Two-Way Transmission With Perturbation

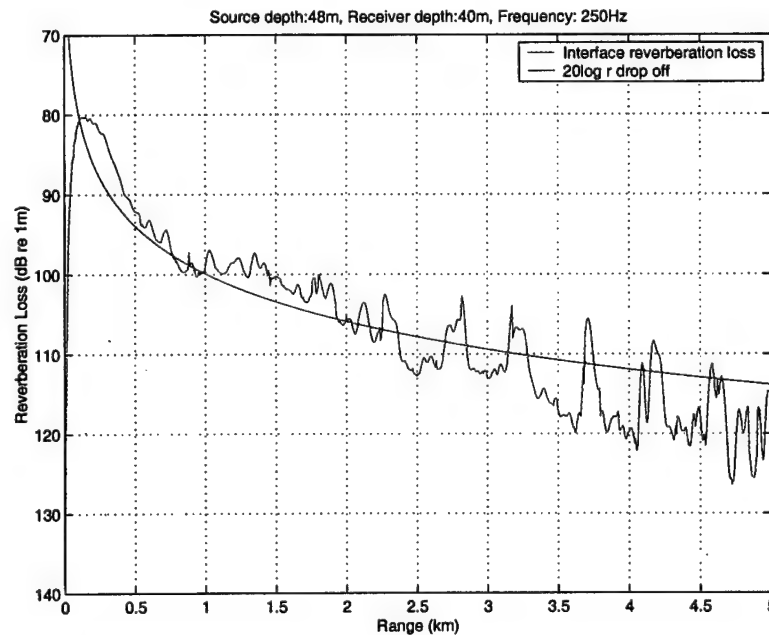


Figure 4.5 – Volume Reverberation Loss for Two-Way Transmission With Perturbation

A comparison between perturbed and unperturbed data was also done. Figures 4.6 and 4.7 show the difference (perturbed RL minus unperturbed RL) to see the fine-scale structures due to the introduction of the perturbation. Apparent in these plots are repeating structures at about every 0.5 km for ranges beyond about 2 km.

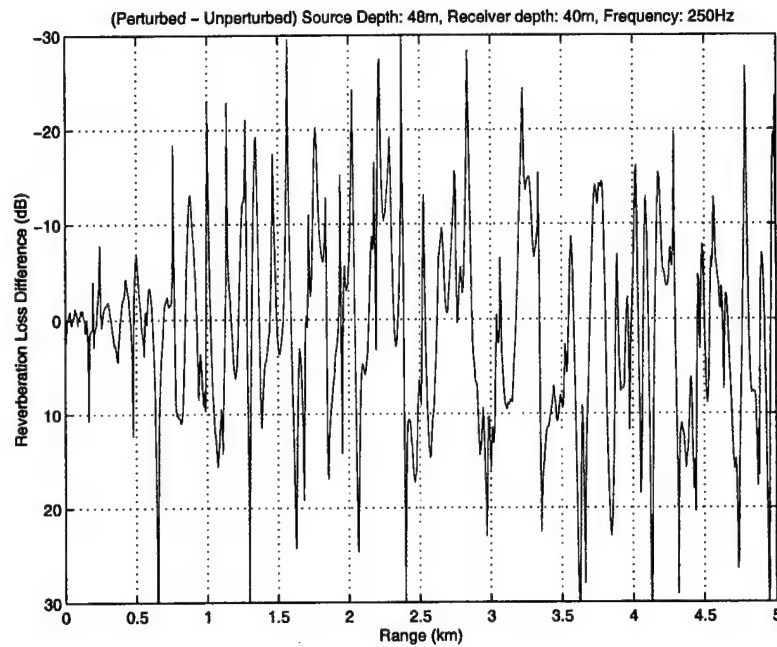


Figure 4.6 – Interface Reverberation Loss Difference Vs Range

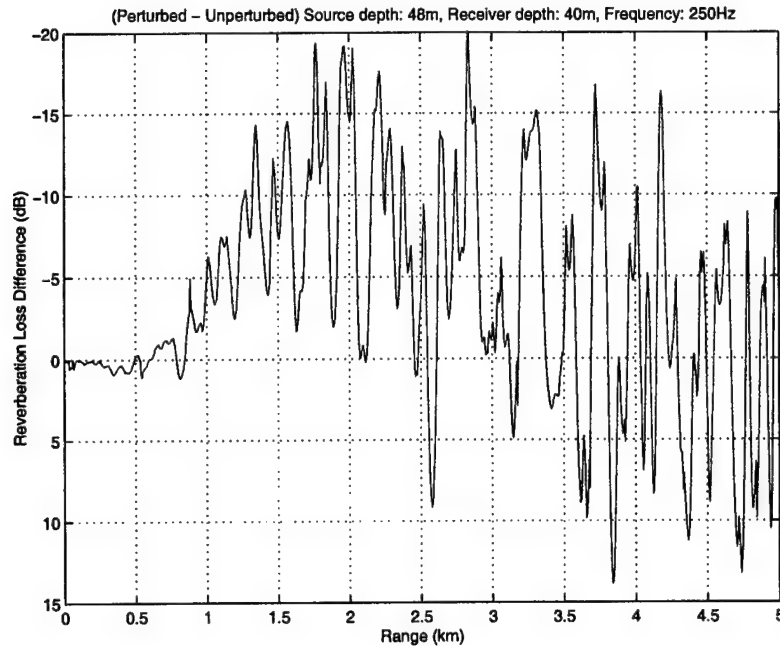


Figure 4.7 – Volume Reverberation Loss Difference Vs Range

Figures 4.8 and 4.9 show the interface and volume reverberation loss, respectively, across depths plotted against range for the center frequency of 250 Hz. It was apparent that the interface reverberation showed more structure while volume reverberation seemed more 'blotchy' and revealed little structure. This smudging of data was manifest of the multiple incoherent (magnitude) multiplications computed before vertically summing the reverberation in depth. What was apparent however, was the ' $20\log r$ ' drop in range in both plots.

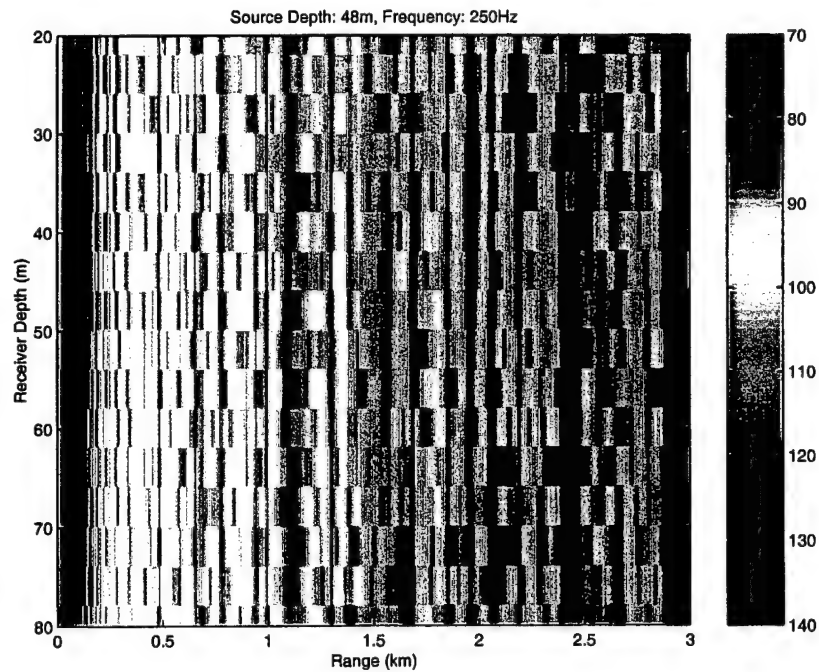


Figure 4.8 – Interface Reverberation Loss (dB re 1 m)
Across Depth Vs Range

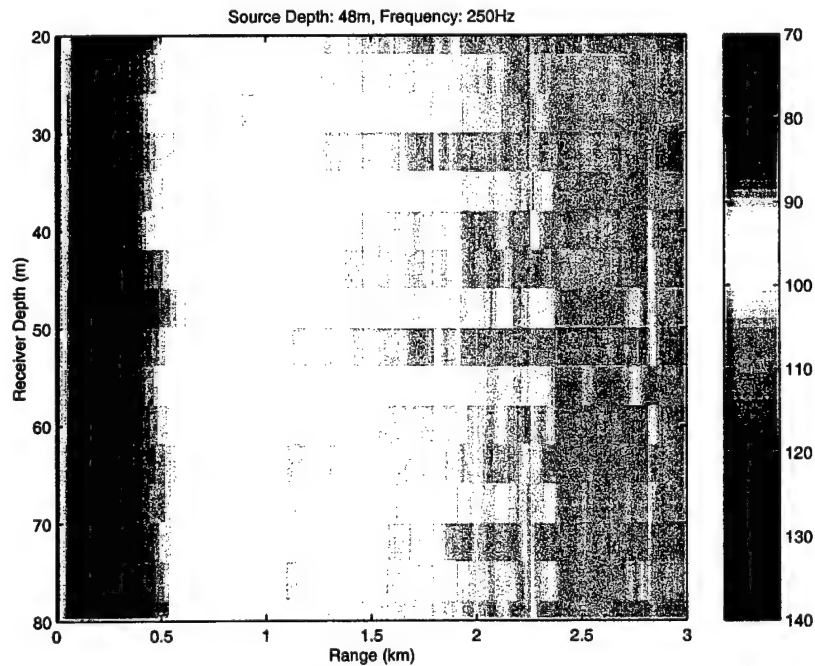


Figure 4.9 – Volume Reverberation Loss (dB re 1 m)
Across Depth Vs Range

3. Two-way Mono/Bistatic Time-Domain Reverberation Analysis

Time-domain analyses for both the interface and volume reverberation were explained in Chapter II, Section C. In essence, multiple frequencies were used to simulate a pulsed propagation. We will use Eqs. (2.68b) and (2.68c) to formulate the MATLAB implementation for the interface and Eqs. (2.70a) to (2.72) for the volume. MMPE was also run based on the same 16 setups for the VLA to provide comparison data for unperturbed data. Implementation was completed using MATLAB with the files created as follows:

MATLAB Post-Processing Files Description	Perturbed Data Processing Files	Unperturbed Data Processing Files
Binary file data extractor: Opens both source and receiver binary files (output from MMPE/MMPEREV). Extracts all modeling parameters and stores them on the MATLAB workspace.	Peout1_bistat.m	peout1_bistat_np.m
Interface and Volume Reverberation Computation: Extracts from binary files the field function data for source and receiver and computes the two-way reverberation loss for the interface and volume as described above.	Peout2way_bistat.m	peout2way_bistat_np.m

Table 4.6 – MATLAB Filenames Created for Time-Domain Reverberation Analysis

The output from each run of peout2way_bistat.m was saved as a MATLAB data file so that the data set could be loaded into the MATLAB workspace without having to re-process the MMPEREV/MMPE output binary files. These are listed in Table 4.7.

Additionally, peout1_bistat.m and peout2way_bistat.m were modified into function form in order to allow unattended batch processing of the transmitter/receiver pairs. MATLAB routines created were: master_run.m, peout1_bifn.m, peout2way_biintfn.m, and peout2way_bivolfn.m, where the interface and volume processing in the original peout2way_bistat.m was split up into two files for processing efficiency.

Receiver Depth	Interface Perturbed Data Ouput	Volume Perturbed Data Ouput	Interface Unperturbed Data Ouput	Volume Unperturbed Data Ouput
20m	bistat4820int.mat	bistat4820vol.mat	bistat4820int_np.mat	bistat4820vol_np.mat
24m	bistat4824int.mat	bistat4824vol.mat	bistat4824int_np.mat	bistat4824vol_np.mat
28m	bistat4828int.mat	bistat4828vol.mat	bistat4828int_np.mat	bistat4828vol_np.mat
32m	bistat4832int.mat	bistat4832vol.mat	bistat4832int_np.mat	bistat4832vol_np.mat
36m	bistat4836int.mat	bistat4836vol.mat	bistat4836int_np.mat	bistat4836vol_np.mat
40m	bistat4840int.mat	bistat4840vol.mat	bistat4840int_np.mat	bistat4840vol_np.mat
44m	bistat4844int.mat	bistat4844vol.mat	bistat4844int_np.mat	bistat4844vol_np.mat
48m	bistat4848int.mat	bistat4848vol.mat	bistat4848int_np.mat	bistat4848vol_np.mat
52m	bistat4852int.mat	bistat4852vol.mat	bistat4852int_np.mat	bistat4852vol_np.mat
56m	bistat4856int.mat	bistat4856vol.mat	bistat4856int_np.mat	bistat4856vol_np.mat
60m	bistat4860int.mat	bistat4860vol.mat	bistat4860int_np.mat	bistat4860vol_np.mat
64m	bistat4864int.mat	bistat4864vol.mat	bistat4864int_np.mat	bistat4864vol_np.mat
68m	bistat4868int.mat	bistat4868vol.mat	bistat4868int_np.mat	bistat4868vol_np.mat
72m	bistat4872int.mat	bistat4872vol.mat	bistat4872int_np.mat	bistat4872vol_np.mat
76m	bistat4876int.mat	bistat4876vol.mat	bistat4876int_np.mat	bistat4876vol_np.mat
80m	bistat4880int.mat	bistat4880vol.mat	bistat4880int_np.mat	bistat4880vol_np.mat

Table 4.7 – Processed Output Data Files in Time-Domain Analysis

4. Time-Domain Analysis Results

Having discussed the implementations, we now show some results obtained. First, we looked at the general structure of interface and volume reverberation in the time-domain at a particular depth chosen arbitrarily as 40 m. Showing very much the same characteristics, Figures 4.10 and 4.11 depict the time-domain interface and volume reverberation loss, respectively. The figures provide an understanding of the structure of the reverberation return of a pulsed transmission with returns lasting for the entire extent of the calculations both in the interface and volume.

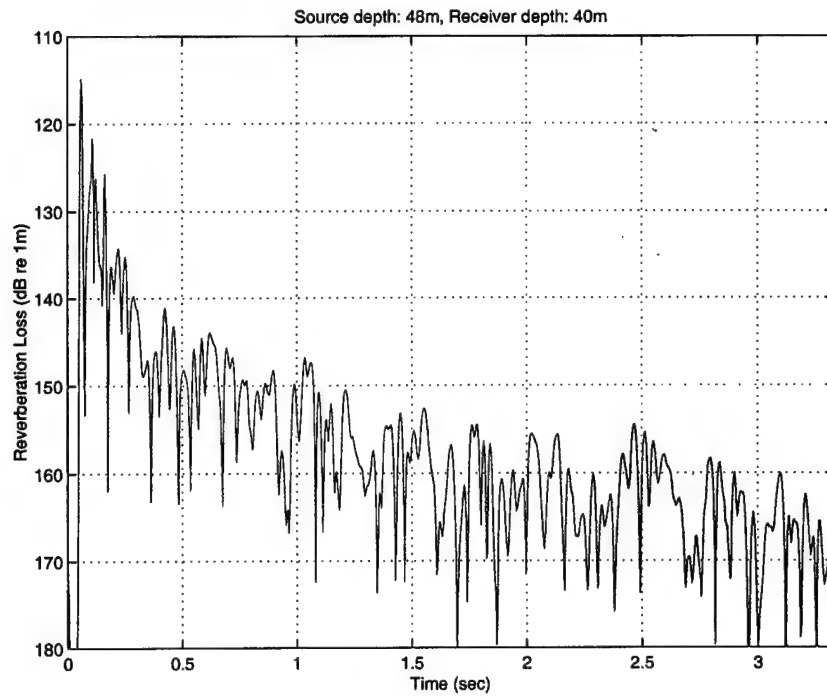


Figure 4.10 – Time-Domain Interface Reverberation Loss
for Two-Way Transmission With Perturbation

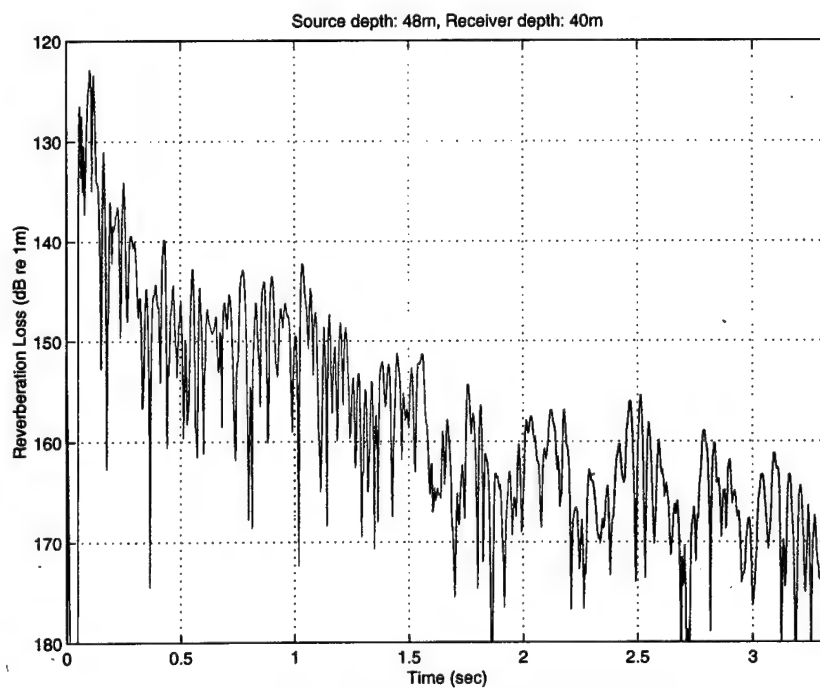


Figure 4.11 – Time-Domain Volume Reverberation Loss
for Two-Way Transmission With Perturbation

Time-domain data sets were also used to provide useful comparisons with unperturbed data sets. To do so, the time axis was 'converted' to a range axis by use of the reference sound speed, c_0 , such that $range = c_0 \times time$. This produced a range axis from 0 to 5 km. The data comparison then proceeded along the same path as that in the CW analysis in the previous section. We first show sample time-series computed reverberation-range plots for the interface and volume. Shown in Figures 4.12 and 4.13 are the time-domain reverberation loss plots equivalent to Figures 4.4 and 4.5 for the CW analyses. Again, the ' $20\log r$ ' drop off was apparent.

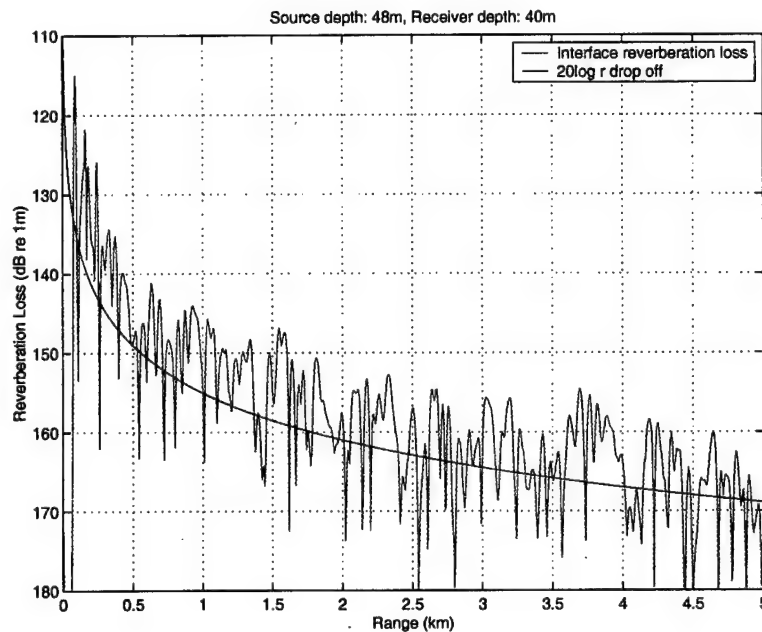


Figure 4.12 –Time-Domain Converted Interface Reverberation Loss (dB re 1 m) Vs Range, With Perturbation

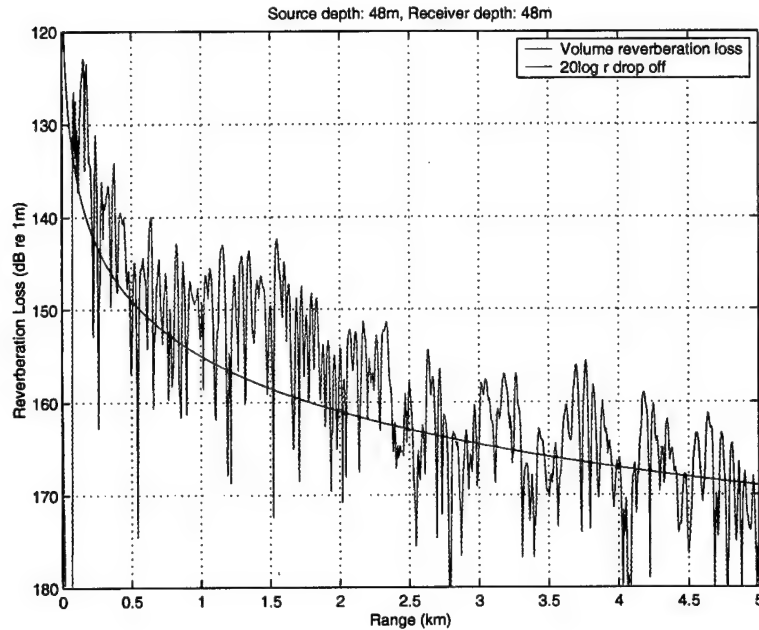


Figure 4.13 – Time-Domain (Converted to Range)
Volume Reverberation Loss Vs Range, With Perturbation

Now looking across depths, we observe multipath structures shown in Figures 4.14 and 4.15 due to both interface and volume perturbations, as expected. Spatial disposition of each source was important in observing the arrival time of the first returns, most apparent at the receiver element at 20 m depth, while arrivals were earlier at the receiver element at 80 m depth. This was due simply to the closer proximity of the deep receiver to the bottom thereby receiving returns earlier than the shallow receivers. No other structures were apparent from these two figures.

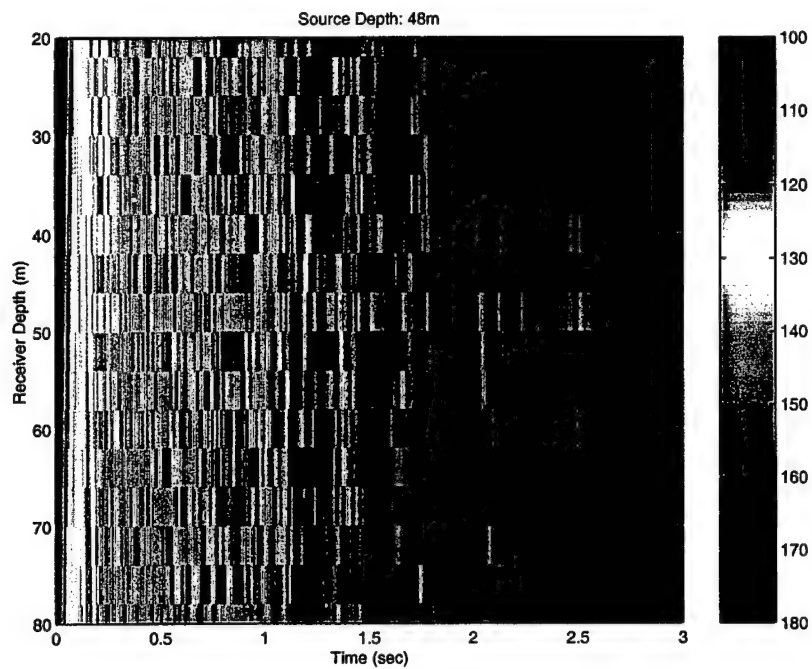


Figure 4.14 – Interface Reverberation Loss Across Depth Vs Time

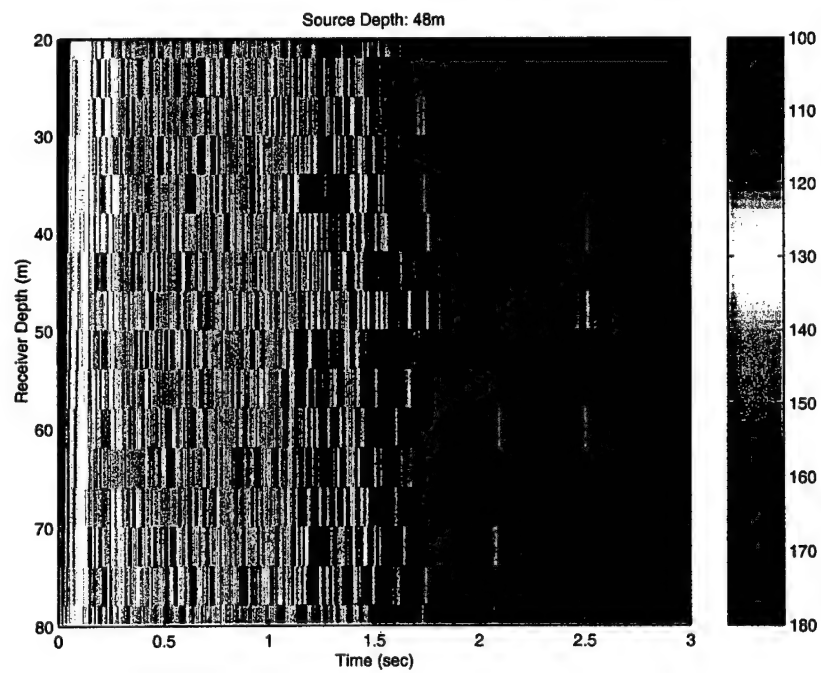


Figure 4.15 – Volume Reverberation Loss Across Depth Vs Time

5. MATLAB Data Analysis

As a final note on the work done in both data and signal analyses, several MATLAB files were also written to ensure that the data analysis was complete. These are found in Table 4.8. In order to derive further value, vertical correlations and spectral analyses were performed. These are discussed in the next sections.

MATLAB Post-Processing Files Description	MATLAB Files
Range-Series Data Processor: Using data obtained from the output file created by peout31_pre_bistat_r.m and peout31_pre_bistat_r_np.m respectively, this routine computes and displays reverberation loss and compares these RLs between perturbed and unperturbed range-series data.	range_series_datanalysis.m
Time-Series Data Processor: Using data obtained from the output file created by peout31_pre_bistat_r.m and peout31_pre_bistat_r_np.m respectively, this routine computes and displays reverberation loss and compares these RLs between perturbed and unperturbed range-series data.	time_series_datanalysis.m

Table 4.8 – MATLAB Routines Created for Data Analyses and Comparisons

C. POST-PROCESSING 2 – VERTICAL CORRELATION & PEAK CORRELATION IN CW AND TIME-DOMAIN

Having completed CW and time-domain analyses, correlation between the monostatic (source and receiver co-located at 48 m) reverberation data set with reverberation data sets from all other receiver depths was performed. The data files saved from the CW (Table 4.5) and time-domain (Table 4.7) analyses were used to compute the vertical correlations for both CW (range correlation) and time-domain (temporal correlation). MATLAB routines were written to perform the vertical correlations. All vertical correlations are computed relative to a source depth of 48 m. Thus, the autocorrelation would occur at the receiver depth of 48 m, giving the theoretical maximum correlation over depth. These were done for both the interface and volume with and without perturbations. Selected results are shown in this section.

1. Vertical Correlation in Range & Peak Vertical Correlation

We first looked at CW vertical correlation. Table 4.9 lists the MATLAB files created to compute the vertical correlations. We have selected a source at 48 m and at the center frequency of 250 Hz for this analysis. With the perturbation included, Figure 4.16 shows the vertical correlation for the interface while Figure 4.17 shows that in the case of the volume. It should be noted that due to the incoherent processing of the two-way pressure fields, the first 0.5 km does not accurately reflect the true reverberation loss. Hence, the first 0.5 km has been truncated prior to performing the volume vertical correlations shown in Figure 4.17.

MATLAB Post-Processing Files Description	MATLAB Files (Perturbed)	MATLAB Files (Unperturbed)
Correlation Computation: Extracted data from Table 4.5 and computed vertical and peak vertical correlations with the data at source depth, 48m.	Peout3_bistat_r.m	peout3_bistat_r_np.m
Data Processing: Extracted data from Table 4.5 and stored workspace variables into an output data file for future analyses.	Peout31_pre_bistat_r.m	peout31_pre_bistat_r_np.m
Correlation Computation: Computes vertical and peak vertical correlations as in peout3_bistat_r.m and peout3_bistat_r_np.m respectively, but uses output file created by peout31_pre_bistat_r.m and peout31_pre_bistat_r_np.m respectively.	Peout31_bistat_r.m	peout31_bistat_r_np.m
Output filename created by peout31_pre_bistat_r.m and peout31_pre_bistat_r_np.m respectively	Bistat_deprng_data.mat	bistat_deprng_np_data.mat

Table 4.9 – MATLAB Filenames Created for Computing Vertical Correlations

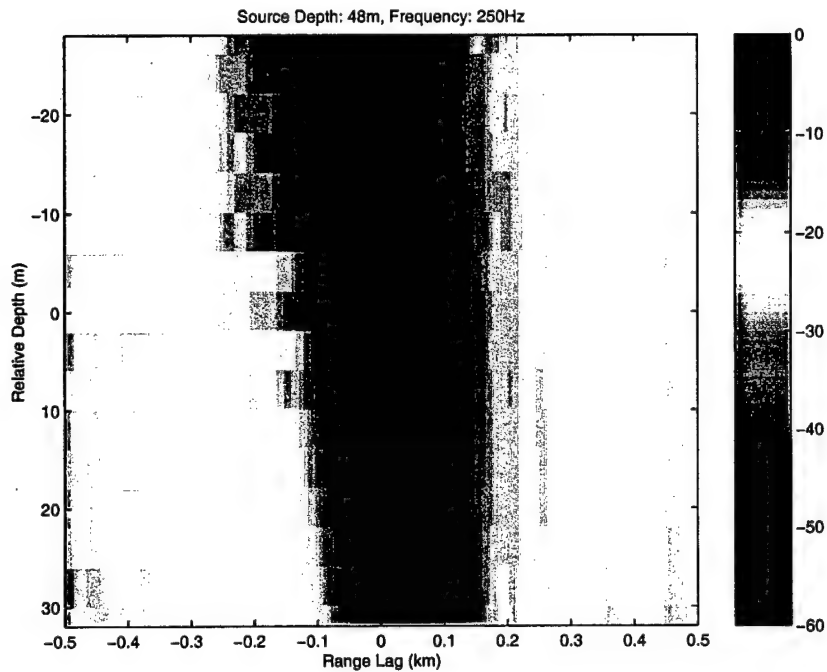


Figure 4.16 – Vertical Correlation of Interface Reverberation Loss in Range Vs Relative Depth

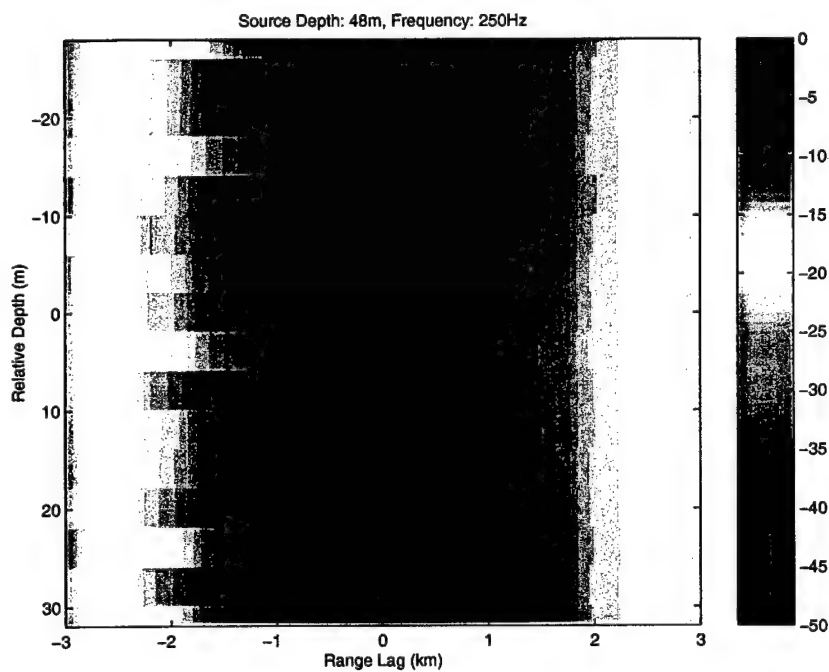


Figure 4.17 – Vertical Correlation of Volume Reverberation Loss in Range Vs Relative Depth (first 0.5km truncated)

It was apparent that finer scale structures were present in the interface, but the volume showed strong correlation throughout depth for much of the computations in range up to about 3 km due to the smoothing effect of the incoherent processing of the CW signal.

Peak correlation values were also extracted from the above vertical correlation structures in order to see how rapidly the signal decorrelated over depth. As would be expected from the above analysis, the volume would tend to stay more correlated over depth while the interface showed more decorrelation over depth. However, even the interface reverberation loss remained quite correlated with minimum correlation values down only about 1 dB. This is also due presumably to the incoherent processing involved in the derivation of the mean squared RPL. Figures 4.18 and 4.19 show a comparison of the peak vertical correlations between perturbed and unperturbed data. While it is apparent that the volume reverberation of the CW signal tends to decorrelate slower than the interface in both scenarios, the addition of the perturbations does not appear to affect the vertical correlations significantly.

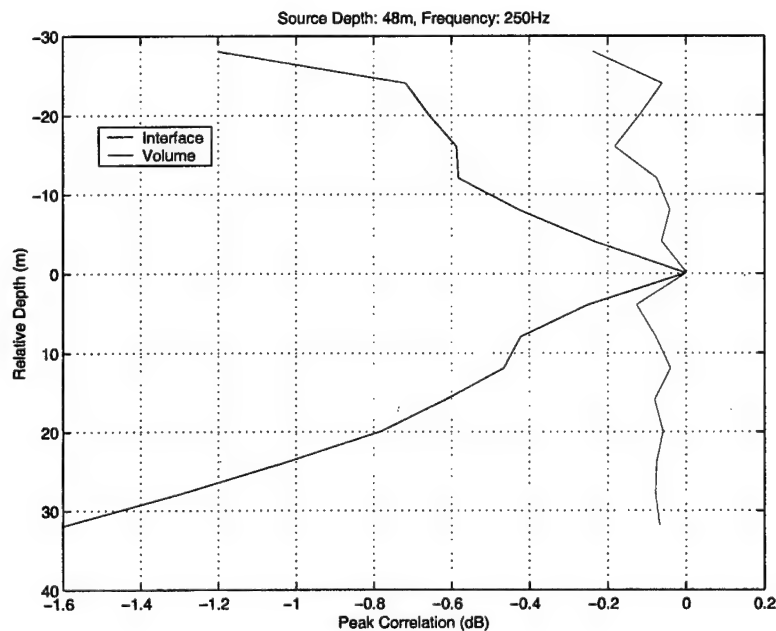


Figure 4.18 – Peak Vertical Correlations (dB) of Perturbed Data Over Relative Depth

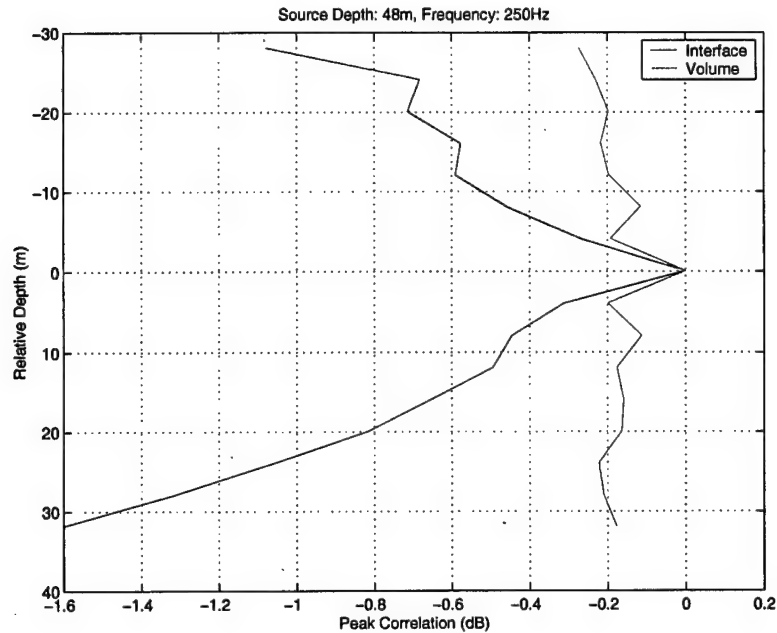


Figure 4.19 – Peak Vertical Correlations (dB) of Unperturbed Data Over Relative Depth

2. Vertical Temporal Correlation & Peak Vertical Temporal Correlation

As with the CW signals, MATLAB files were created to compute the vertical correlations in the time-domain for the broadband signals. These are listed in Table 4.9. From the results of the vertical temporal correlations and peak vertical temporal correlations, we obtain Figures 4.20 through 4.23.

Apparent from Figures 4.20 and 4.21 are finer scale structures seen in both the interface and volume reverberation level. Of importance was the fact that the coherent convolution done in arriving at the time-domain analysis preserved the coherent time structures, in contrast to the CW analyses.

MATLAB Post-Processing Files Description	MATLAB Files (Perturbed)	MATLAB Files (Unperturbed)
Correlation Computation: Extracted data from Table 4.7 and computed vertical and peak vertical correlations with the data at source depth, 48m.	peout3_bistat.m	peout3_bistat_np.m
Data Processing: Extracted data from Table 4.7 and stored workspace variables into an output data file for future analyses.	peout31_pre_bistat.m	peout31_pre_bistat_np.m
Correlation Computation: Computes vertical and peak vertical correlations as in peout3_bistat.m and peout3_bistat_np.m respectively, but uses output file created by peout31_pre_bistat.m and peout31_pre_bistat_np.m respectively.	peout31_bistat.m	peout31_bistat_np.m
Output filename created by peout31_pre_bistat.m and peout31_pre_bistat_np.m respectively	bistat_deptime_data.mat	bistat_deptime_np_data.mat

Table 4.10 – MATLAB Filenames Created for Computing Vertical Correlations

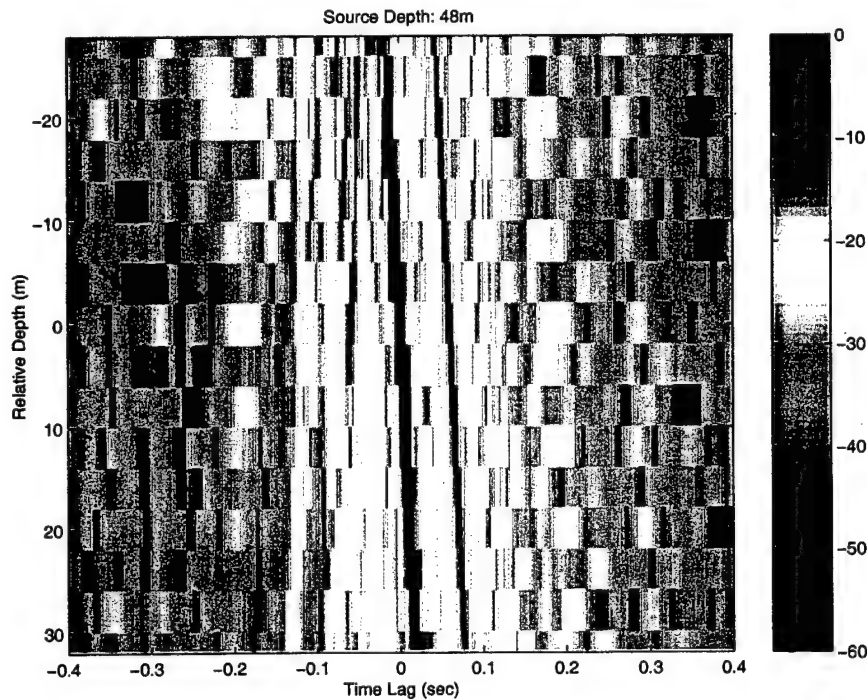


Figure 4.20 – Vertical Temporal Correlation of Interface Reverberation Loss Vs Relative Depth

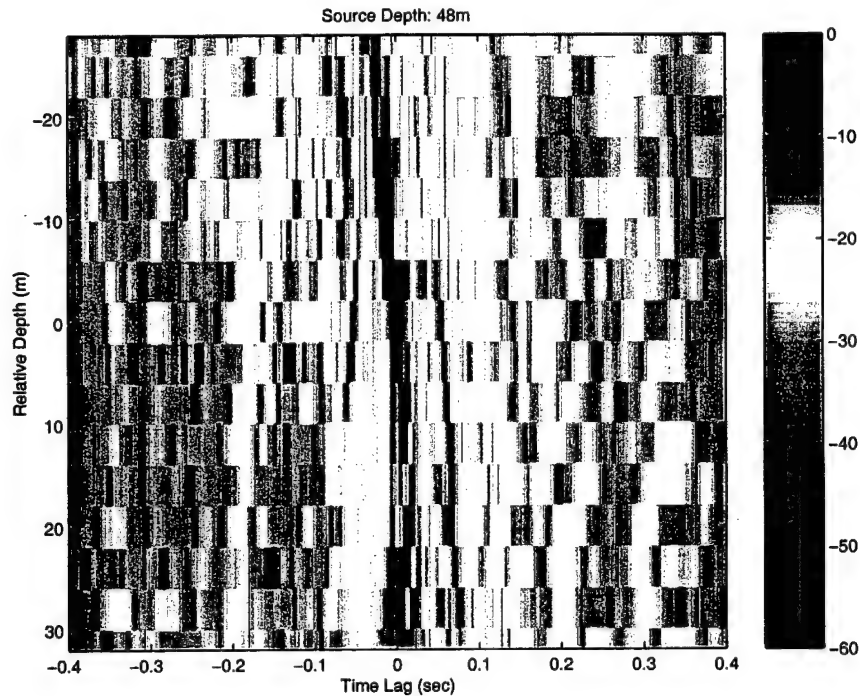


Figure 4.21 – Vertical Temporal Correlation of Volume Reverberation Loss Vs Relative Depth

Peak vertical temporal correlations were extracted for the interface and volume relative to a 48m source, and the results are displayed in Figure 4.22. Similar analysis was performed on data computed without the perturbations and these results are presented in Figure 4.23. With the same horizontal scales, Figures 4.22 and 4.23 could be compared to see the effects of introducing perturbations. The perturbations appear to affect the volume reverberation loss vertical correlation more than the interface reverberation loss, although the effect is minor in both cases. For both perturbed and unperturbed environments, the vertical 3dB decorrelation length scale is on the order of a few meters.

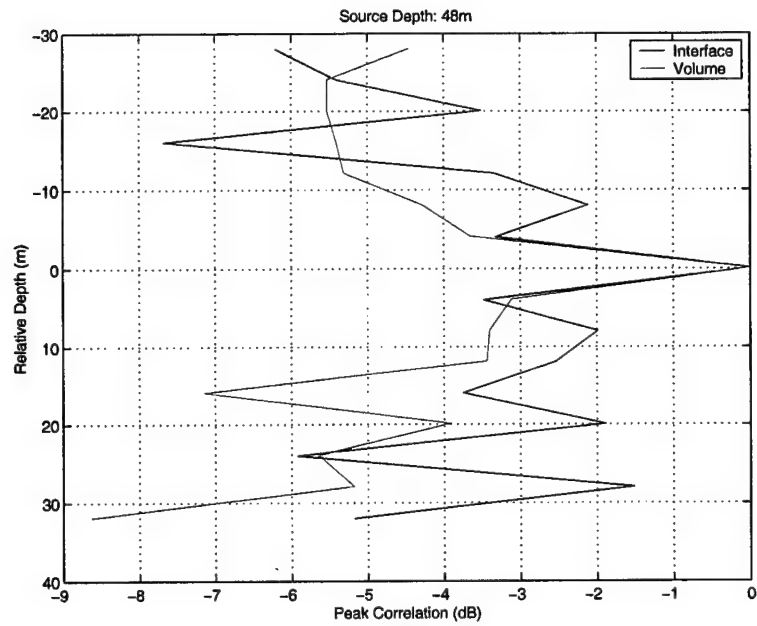


Figure 4.22 – Peak Vertical Temporal Correlations of Perturbed Data

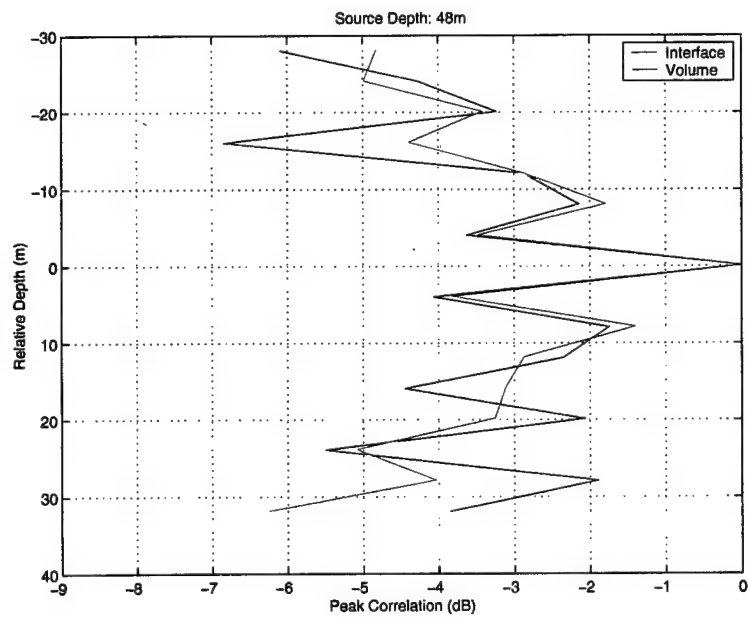


Figure 4.23 – Peak Vertical Temporal Correlations of Unperturbed Data

D. POST-PROCESSING 3 – SPECTRAL ANALYSES

In this final section, we investigate the spectral content of the reverberation pressure obtained for both the CW and broadband signals. There was a need to convert the time-domain into range using the reference sound speed, c_0 , like the conversion done in Section 3.B in the time-domain analysis. As before, comparison with unperturbed data was also done. MATLAB routines were again written and tabulated as follows.

MATLAB Post-Processing Files Description	MATLAB Files
Computes the Fourier Transform of the CW data obtained from the output file created by peout31_pre_bistat.m and peout31_pre_bistat_np.m respectively. This analysis has built within itself a comparison with unperturbed data already.	range_series_signalysis.m
Computes the Fourier Transform of the Converted Time-Domain data obtained from the output file created by peout31_pre_bistat.m and peout31_pre_bistat_np.m respectively. This analysis has built within itself, a comparison with unperturbed data already.	time_series_signalysis.m

Table 4.11 – MATLAB Routines Created for Spectral Decomposition

Assuming a monostatic geometry, we recall from the analyses in Chapter II and from Eqs. (4.15) and (4.16) that the interface reverberation loss may be defined as

$$RL_b = 2TL_b + constants \quad , \quad (4.17)$$

where

$$TL_b = 10 \log |p_-(r)|^2 = 20 \log |\psi_b(r)| - 10 \log r \quad (4.18)$$

since, by definition,

$$|p(r)| = \frac{1}{\sqrt{r}} |\psi(r)|. \quad (4.19)$$

Hence

$$RL_b \propto 20 \log |\psi_b(r)|^2 - 20 \log r. \quad (4.20)$$

We define the range-reduced reverberation loss as

$$RL_{b, reduced} = RL_b + 20 \log r \propto 20 \log |\psi_b(r)|^2. \quad (4.21)$$

Now we assume that we can represent the field function in terms of a spectrum, i.e.

$$|\psi_b(r)|^2 \propto \int W(K) e^{iKr} dK. \quad (4.22)$$

It is possible then that the spectral content of the field can be related to the statistical characteristics of the perturbations and can thus be extracted with the use of some signal processing tools. In other words, the spectrum $W(K)$ may be related to the perturbation spectra.

The main approach was the use of discrete Fourier transforms (DFT) in an attempt to extract the spectral components of the reverberation data. They are:

- Signal Analysis 1: Power Spectral Density – DFT of the magnitude squared range-reduced reverberation (i.e. $r^2 \times |p_-|^2$).
- Signal Analysis 2: Power Ratio Spectral Density – DFT of the magnitude squared of the ratio of the reverberation (perturbed divided by unperturbed),

$$\text{i.e., } \frac{|p_{\text{-perturbed}}|^2}{|p_{\text{-unperturbed}}|^2}.$$

Recall that the typical reverberation loss observed from the range series (CW) data for the interface and volume were presented earlier in this chapter in Figures 4.4 and 4.5 respectively. The time-domain reverberation loss data was correspondingly shown in Figures 4.10 and 4.11. The difference in RL (ratio) between the perturbed and unperturbed data (CW analysis) for the interface and volume were also shown in Figures 4.6 and 4.7. Figures 4.24 and 4.25 show the CW reverberation loss while Figures 4.26 and 4.27 show the time-domain (converted to range) reverberation loss.

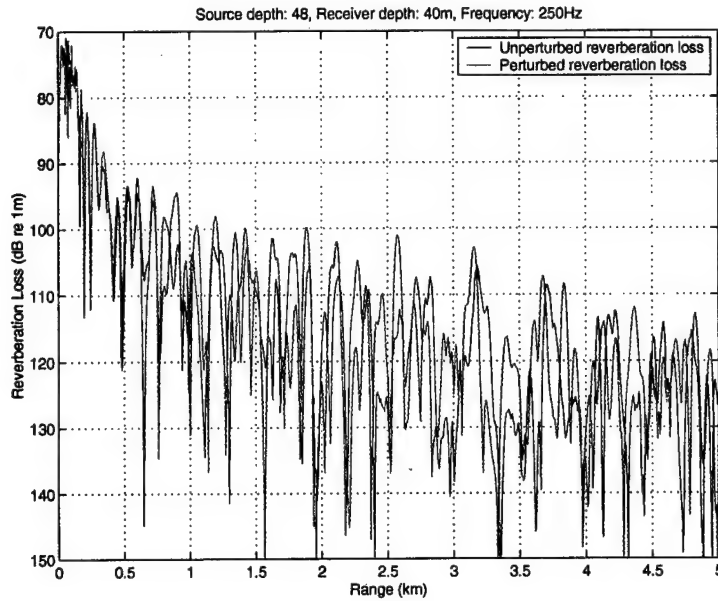


Figure 4.24 – Interface Reverberation Loss vs Range Using Range Series Data

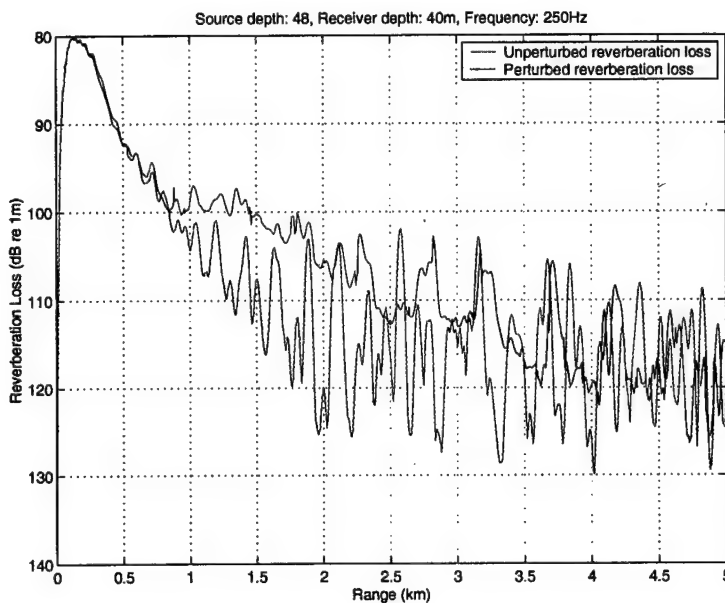


Figure 4.25 – Volume Reverberation Loss vs Range Using Range Series Data

When using time-series data to perform this analysis, time was converted to range in order to relate length scales of the reverberation with perturbation scales. It is perhaps interesting to note that the time-series data showed no appreciable differences between

the perturbed and unperturbed data sets, in contrast to the CW range-series data displayed above. The reason for this is currently unknown.

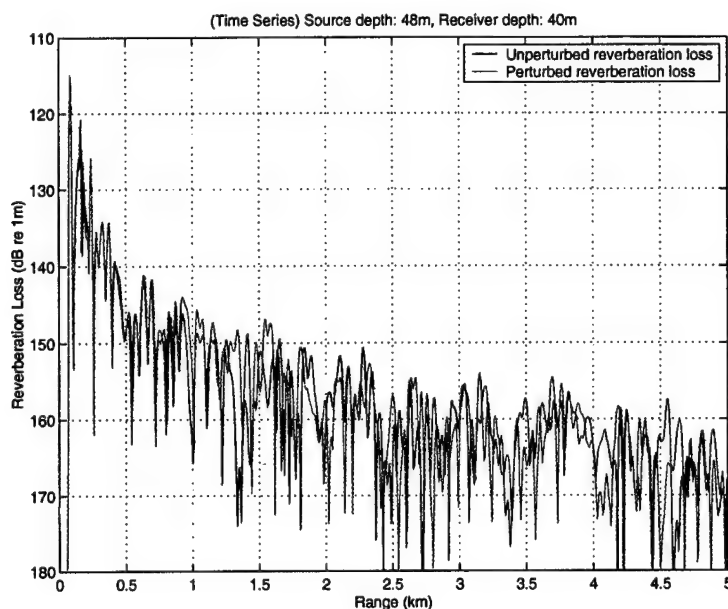


Figure 4.26 – Interface Reverberation Loss (dB re 1 m) vs Range Using Time Series Data

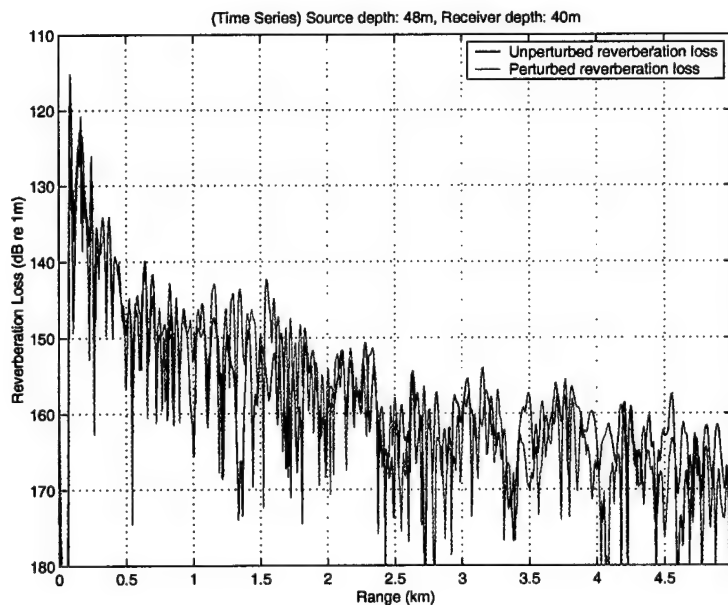


Figure 4.27 – Volume Reverberation Loss (dB re 1 m) vs Range Using Time Series Data

1. Signal Analysis 1 – Power Spectral Density

The magnitude-squared of the range-reduced perturbed reverberation was analyzed using the DFT, giving

$$PSD = DFT\{|p_-|^2 \times r^2\} \quad (4.23)$$

where p_- is the reverberation field of the interface or volume. Figures 4.28 and 4.29 show the normalized power spectrum of the range-reduced interface and volume reverberations, respectively. Note that these plots are presented with the wavenumber axis displayed on a logarithm scale in order to elucidate exponential behavior. While structurally the same, i.e., lower wavenumbers predominating the spectra, strong fine scale structures were evident in both plots for the perturbed data. This alludes to the presence of perturbations which may be extracted from the spectra. In the volume plot, Figure 4.29, the perturbed data distinctly showed less drop-off beyond a wavenumber of roughly 0.2 m^{-1} corresponding to wavelengths smaller than approximately 30 m.

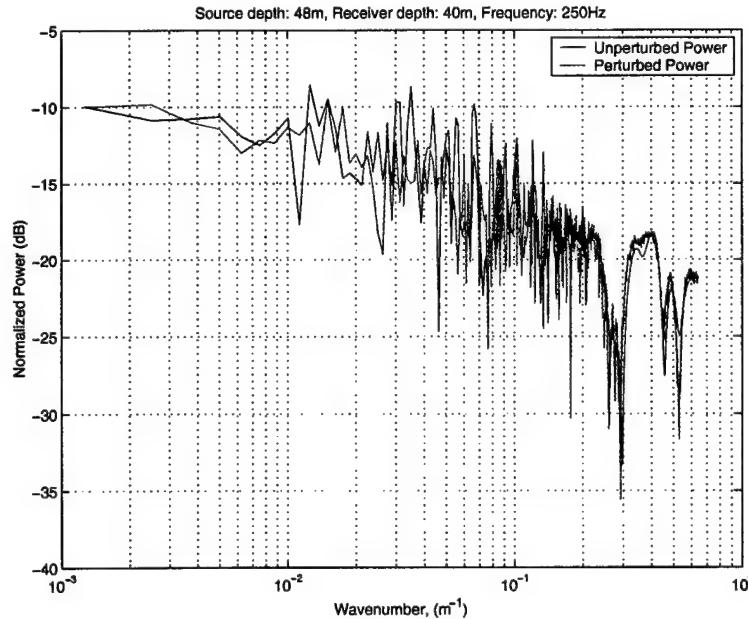


Figure 4.28 – Normalized Power Spectrum of Range-Reduced Interface Reverberation (Range-Series)

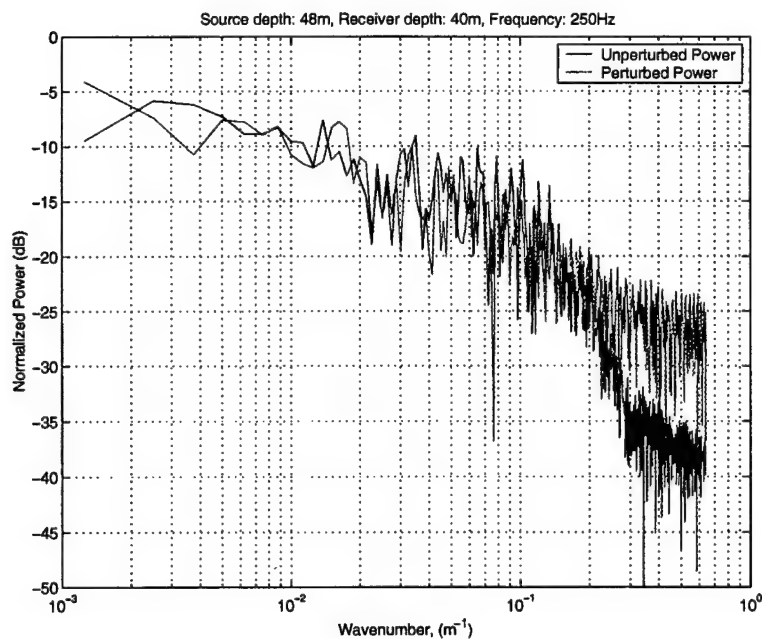


Figure 4.29 – Normalized Power Spectrum of Range-Reduced Volume Reverberation (Range-Series)

Figures 4.30 and 4.31 show the results for the broadband signal (after converting time to range) for the interface and volume. Both fine and large scale structures are observed. While repeating structures were mostly preserved when the perturbation was included, the longer scale perturbations may have augmented the spectra.

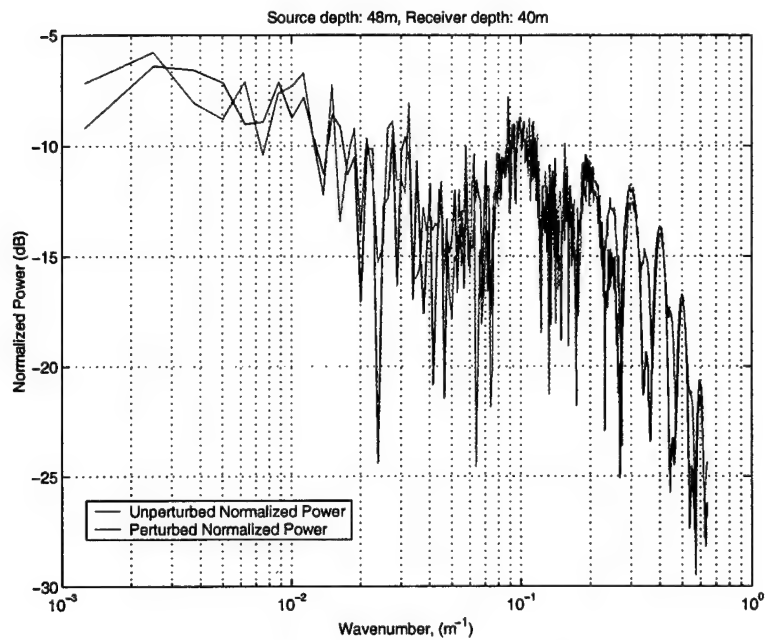


Figure 4.30 – Normalized Power Spectrum of Range-Reduced Broadband Interface Reverberation

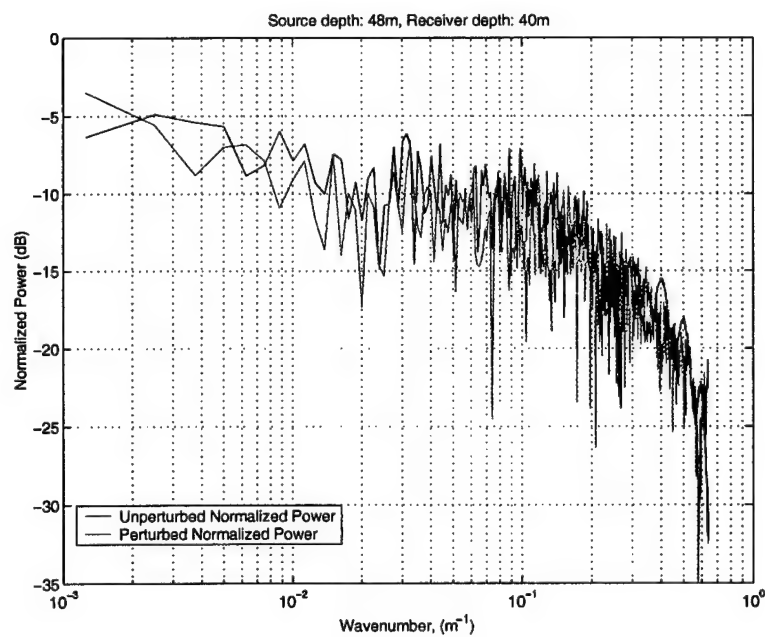


Figure 4.31 – Normalized Power Spectrum of Range-Reduced Broadband Volume Reverberation

2. Signal Analysis 2 – Power Ratio Spectral Density

The quotient of the perturbed over the unperturbed reverberation data was magnitude-squared to provide a comparison of the levels. This was then Fourier transformed in order to reveal any special spectral content. The power ratio spectral density (*PRSD*) was then defined as

$$PRSD = DFT \left\{ \frac{|P_{-perturbed}|^2}{|P_{-unperturbed}|^2} \right\}. \quad (4.24)$$

Figures 4.32 and 4.33 show the spectral components of the ratio between the perturbed and unperturbed data sets for the CW signal. While it was difficult to make any apparent observations, the interface reverberation data showed a rather flat spectrum while the volume reverberation data showed a roll-off at higher wavenumbers. The physical justification for this is, as yet, unclear.

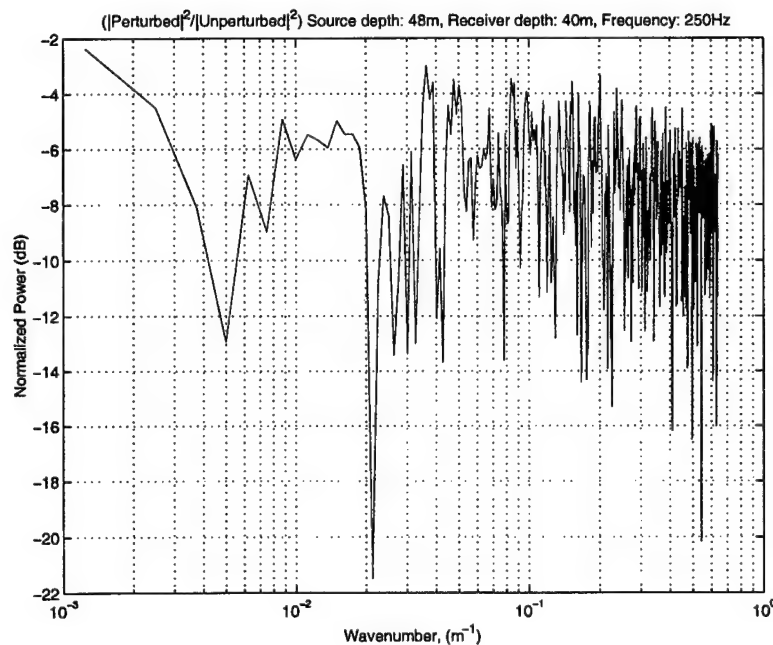


Figure 4.32 – Normalized Spectrum of Interface Power Ratio Using Range-Series Data

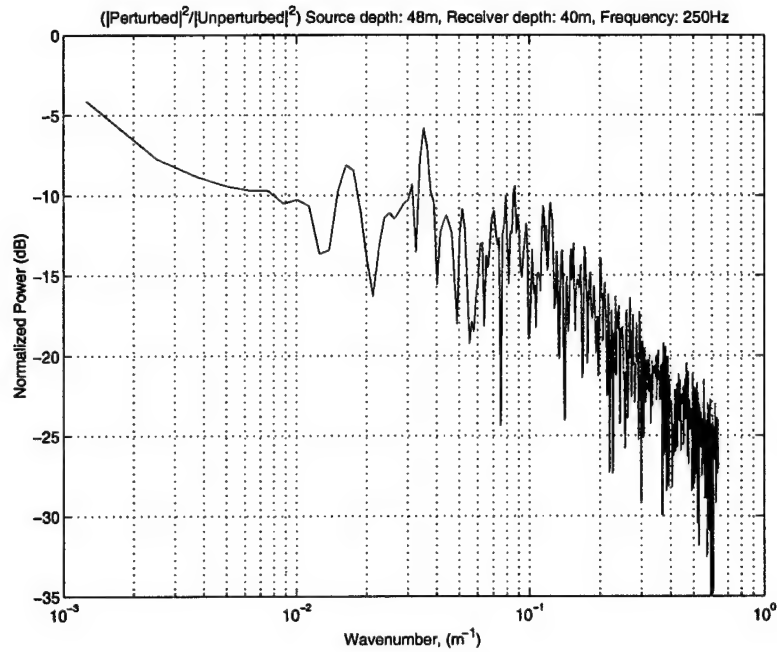


Figure 4.33 – Normalized Spectrum of the Volume Power Ratio
Using Range-Series Data

Finally, we computed the power ratio spectral density based on the time-series data, as shown in Figures 4.34 and 4.35 for the interface and volume, respectively. These plots were consistent with the above CW analysis for the ratio of the perturbed to the unperturbed data. The interface showed an almost flat spectra while the volume showed a drop-off with increasing wavenumber.

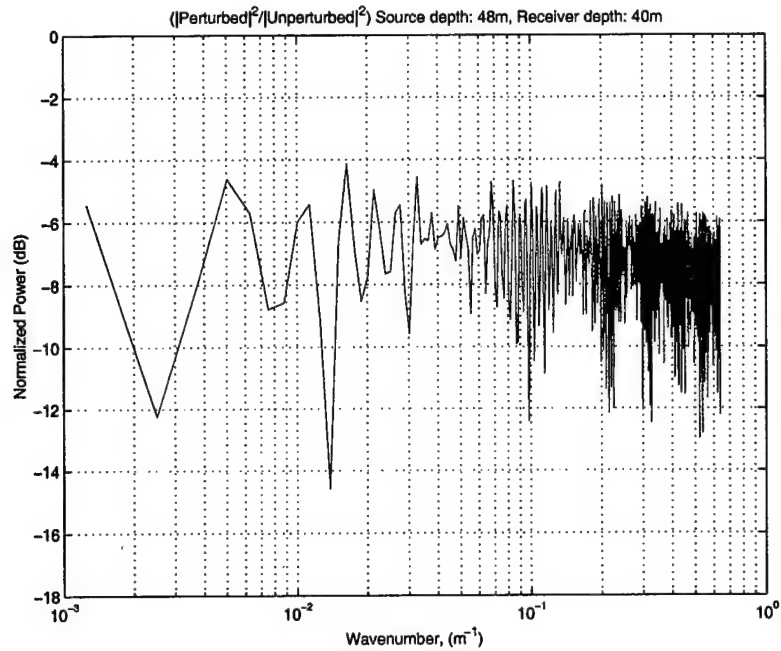


Figure 4.34 – Normalized Spectrum of Interface Power Ratio
Using Time-Series Data

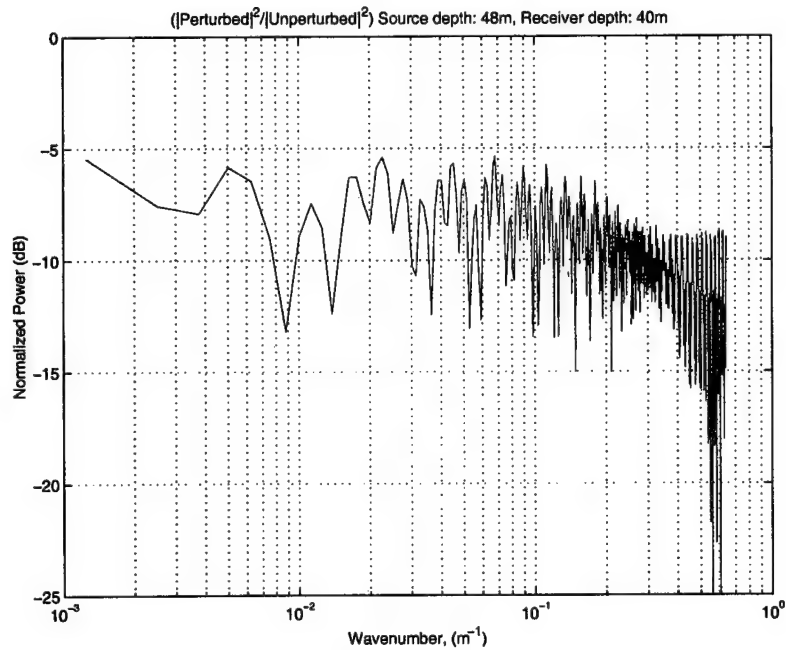


Figure 4.35 – Normalized Spectrum of Volume Power Ratio
Using Time-Series Data

THIS PAGE IS INTENTIONALLY LEFT BLANK

V. CONCLUSIONS & RECOMMENDATIONS

A theoretical model and corresponding numerical simulation for shallow water reverberation has been developed for spatial and sound speed perturbations of the bottom interface and volume, in the context of the parabolic approximation. The main focus in this thesis has been the use of the MMPE model for predicting the forward and back propagations, and then developing post-processing routines in MATLAB to compute the reverberation loss and to perform signal analyses on the derived reverberation.

The development of statistical models to introduce interface and volume perturbations into the MMPE model were also completed, noting that density variations to the volume have yet to be included to arrive at a more comprehensive model. This is, however, not envisaged to be difficult and will be left for follow-on work. The models presented here were tested and found to be effective in modeling the perturbations typical of different types of bottoms and sediment compositions. An rms value of 1 m interface perturbation and a 15 m/s sound speed variation were used. Most apparent was the effect these perturbations had on a one-way propagation of the MMPE model. It showed diffused bottom penetration extending much farther in range with less noticeable effects in the water column.

Various analyses were conducted for both perturbed and unperturbed environments in order to establish baselines for which to see the effects of perturbation. This was done in computing the reverberation losses across a VLA based on a single source located at range, $r = 0$ m, and at 48 m depth. Arrival structures were clearly discernible due to travel time differences, the shallowest receivers showing later arrival times. Reverberation levels consistently showed '20log r ' drop-offs regardless of the presence of perturbation. Correlation across depth was performed and showed that the interface decorrelated more rapidly than for the volume. This was also true of the

scenario without perturbations. Thus, the perturbations were not seen to affect correlation significantly.

The power spectrum of the reverberation and of the ratio of the perturbed to the unperturbed data were computed. In the power spectral analysis of the volume reverberation, showed less drop-off for the perturbed data. However, both interface and volume-perturbed plots showed small and large-scale deviations from the unperturbed plots, providing evidence of the perturbations. Broadband analysis showed that repeating structures were preserved while shorter scale perturbations may have augmented the spectra. The PRSD showed a rather flat spectrum for the interface reverberation data while volume reverberation showed roll-off at higher wavenumbers. This was consistent in both the CW and broadband analyses but the justification is not presently known.

In essence, we have analyzed the influence of interface and volume perturbations on CW and broadband reverberation structure in shallow water. The impact of the interface perturbations cannot be really concluded at this time since the spectral analyses did not provide any observable characteristics. The volume perturbation spectrum appeared more amenable to extraction via signal processing and should be explored further.

With the conclusion of this thesis, recommendations for future work are:

- to generalize the Fortran implementation of the perturbation models with truly random perturbations by incorporating a 'seed';
- to develop and implement density fluctuations into the sediment volume and reverberation theory;
- and to perform second and third order signal analyses on the reverberation data in an attempt to extract information on the perturbation spectra.

LIST OF REFERENCES

1. Brekhovskikh, L.M. and Lysanov, Y. P. (1990). *Fundamentals of Ocean Acoustics, Second Edition*, Springer-Verlag, New York, pp. 183–186.
2. Goff, J. A. and Jordan, T. H. (1988). "Stochastic modeling of seafloor morphology: Inversion of Sea Beam data for second-order statistics," *J. Geophys. Res.* 93, 13589-13609.
3. Jensen, F.B., Kuperman, W.A., Porter, M.B. and Schmidt, H. (1994). *Computational Ocean Acoustics*, AIP Press, Woodbury, New York, pp. 78–80.
4. Makris, N.C. and Berkson, J.M. (1994). "Long-range backscatter from the Mid-Atlantic Ridge," *J. Acoust. Soc. Am.*, Vol. 95, pp. 1865–1881.
5. Smith, K.B. and Tappert, F.D. (1994). "UMPE: The University of Miami Parabolic Equation Model Version 1.1," MPL Technical Memorandum 432, San Diego, California.
6. Smith, K.B., Hodgkiss, W.S. and Tappert, F.D. (1996). "Propagation and analysis issues in the prediction of long-range reverberation," *J. Acoust. Soc. Am.* 99, 1387-1404.
7. Smith, K. B. and Cushman, E.B. (1997). "A comparison of quasi-continuous wave and broadband travel time techniques in the prediction of long-range reverberation," *J. Acoust. Soc. Am.*, Vol. 102 (4) pp. 2063–2071.
8. Smith, K.B. (2000). "Convergence, stability, and variability of shallow water acoustic predictions using a split-step Fourier parabolic equation model," *Proceedings of the Shallow Water Acoustic Modeling (SWAM '99) Workshop*, 8–10 September 1999, *J. Comp. Acoust.* (Special Issue, in press).
9. Tappert, F. D. (1977). "The parabolic approximation method," in *Lecture Notes in Physics*, Vol. 70, *Wave Propagation and Underwater Acoustics* (edited by Keller, J. B. and Papadakis, J. S.), Springer-Verlag, New York, pp. 224–287.
10. Tappert, F.D. and Ryan, F. (1989). "Full-wave bottom reverberation modeling," *J. Acoust. Soc. Am. Suppl.* 86, S65.
11. Thomson, D.J. and Chapman, N.R. (1983). "A wide-angle split-step algorithm for the parabolic equation," *J. Acoust. Soc. Am.*, Supplement Vol. 83, S118.

12. Tucholke, B.E., Kleinrock, M.C. and Stewart, W.K. (1993a). "Geological and Geophysical Characteristics of the Acoustic Reverberation Corridor and their relevance to the Conduct of the G&G Fine-Scale Surveys," ONR-ARSRP Symposium, La Jolla, CA, 23-25 March 1993.
13. Tucholke, B.E., Kleinrock, M.C. and Stewart, W.K. (1993b). "Fine-Scale Geological and Geophysical Surveys at Sites A, B, C, and D in the Acoustic reverberation Corridor," ONR-ARSRP Symposium, La Jolla, CA, 1-3 December 1993.
14. Yamamoto, T. (1995). "Velocity variabilities and other physical properties of marine sediments measured by crosswell acoustic tomography," J. Acoust. Soc. Am., Vol. 98 (4) pp. 2235-2248.

INITIAL DISTRIBUTION LIST

1. Defense Technical Information Center.....2
 8725 John J. Kingman Rd., STE 0944
 Ft. Belvoir, VA 22060-6218

2. Dudley Knox Library.....2
 Naval Postgraduate School
 411 Dyer Rd.
 Monterey, CA 93943-5101

3. Prof. Kevin B. Smith, Code PH/Sk.....6
 Department of Physics
 Naval Postgraduate School
 Monterey, CA 93943-5002

4. Prof. James V. Sanders, Code PH/Sd1
 Department of Physics
 Naval Postgraduate School
 Monterey, CA 93943-5002

5. Dr. Jeff Simmen (Code 321OA)1
 Office of Naval Research
 800 N. Quincy Street
 Arlington, VA 22217

6. Dr. Ellen Livingston (Code 321OA).....1
 Office of Naval Research
 800 N. Quincy Street
 Arlington, VA 22217

7. MAJOR Li, Lit Siew.....2
 c/o Overseas Courses Branch
 Naval Training Department
 Headquarters Republic of Singapore Navy
 Ministry of Defence
 SINGAPORE